CrossMark

Early Results from GLASS-JWST. XX. Unveiling a Population of "Red Excess" Galaxies in Abell2744 and in the Coeval Field

Benedetta Vulcani[1], Tommaso Treu[2], Antonello Calabrò[3], Jacopo Fritz[4], Bianca M. Poggianti[1], Pietro Bergamini[5,6], Andrea Bonchi[7], Kristan Boyett[8,9], Gabriel B. Caminha[10,11], Marco Castellano[3], Alan Dressler[12], Adriano Fontana[3], Karl Glazebrook[13], Claudio Grillo[5,14], Matthew A. Malkan[2], Sara Mascia[3], Amata Mercurio[15,16], Emiliano Merlin[3], Benjamin Metha[2,8,9], Takahiro Morishita[17], Themiya Nanayakkara[13], Diego Paris[3], Guido Roberts-Borsani[2], Piero Rosati[6,18], Namrata Roy[19], Paola Santini[3], Michele Trenti[8,9], Eros Vanzella[6], and Xin Wang[20,21,22]

[1] INAF—Osservatorio astronomico di Padova, Vicolo Osservatorio 5, I-35122 Padova, Italy; benedetta.vulcani@inaf.it
[2] Department of Physics and Astronomy, University of California, Los Angeles, 430 Portola Plaza, Los Angeles, CA 90095, USA
[3] INAF—Osservatorio Astronomico di Roma, via di Frascati 33, I-00078 Monte Porzio Catone, Italy
[4] Instituto de Radioastronomia y Astrofisica, UNAM, Campus Morelia, AP 3-72, CP 58089, Mexico
[5] Dipartimento di Fisica, Universitá degli Studi di Milano, via Celoria 16, I-20133 Milano, Italy
[6] INAF—OAS, Osservatorio di Astrofisica e Scienza dello Spazio di Bologna, via Gobetti 93/3, I-40129 Bologna, Italy
[7] Space Science Data Center, Italian Space Agency, via del Politecnico, I-00133, Roma, Italy
[8] School of Physics, University of Melbourne, Parkville, VIC 3010, Australia
[9] ARC Centre of Excellence for All Sky Astrophysics in 3 Dimensions (ASTRO 3D), Australia
[10] Technische Universität München, Physik-Department, James-Franck Str. 1, D-85748 Garching, Germany
[11] Max-Planck-Institut für Astrophysik, Karl-Schwarzschild-Str. 1, D-85748 Garching, Germany
[12] The Observatories, The Carnegie Institution for Science, 813 Santa Barbara St., Pasadena, CA 91101, USA
[13] Centre for Astrophysics and Supercomputing, Swinburne University of Technology, PO Box 218, Hawthorn, VIC 3122, Australia
[14] INAFIASF Milano, via A. Corti 12, I-20133 Milano, Italy
[15] Dipartimento di Fisica "E.R. Caianiello," Universitá Degli Studi di Salerno, Via Giovanni Paolo II, I-84084 Fisciano (SA), Italy
[16] INAF—Osservatorio Astronomico di Capodimonte, Via Moiariello 16, I-80131 Napoli, Italy
[17] IPAC, California Institute of Technology, MC 314-6, 1200 E. California Boulevard, Pasadena, CA 91125, USA
[18] Dipartimento di Fisica e Scienze della Terra, Universitá degli Studi di Ferrara, Via Saragat 1, I-44122 Ferrara, Italy
[19] Center for Astrophysical Sciences, Department of Physics and Astronomy, Johns Hopkins University, Baltimore, MD 21218, USA
[20] School of Astronomy and Space Science, University of Chinese Academy of Sciences (UCAS), Beijing 100049, People's Republic of China
[21] National Astronomical Observatories, Chinese Academy of Sciences, Beijing 100101, People's Republic of China
[22] Institute for Frontiers in Astronomy and Astrophysics, Beijing Normal University, Beijing 102206, People's Republic of China

Abstract

We combine JWST/NIRCam imaging and MUSE data to characterize the properties of galaxies in different environmental conditions in the cluster Abell2744 ($z = 0.3064$) and in its immediate surroundings. We investigate how galaxy colors, morphology, and star-forming fractions depend on wavelength and on different parameterizations of environment. Our most striking result is the discovery of a "red excess" population in F200W−F444W colors in both the cluster regions and the field. These galaxies have normal F115W−F150W colors but are up to 0.8 mag redder than red sequence galaxies in F200W−F444W. They also have rather blue rest-frame $B-V$ colors. Galaxies in the field and at the cluster virial radius are overall characterized by redder colors, but galaxies with the largest color deviations are found in the field and in the cluster core. Several results suggest that mechanisms taking place in these regions might be more effective in producing these colors. Looking at their morphology, many cluster galaxies show signatures consistent with ram pressure stripping, while field galaxies have features resembling interactions and mergers. Our hypothesis is that these galaxies are characterized by dust-enshrouded star formation: a JWST/NIRSpec spectrum for one of the galaxies is dominated by a strong PAH at 3.3 μm, suggestive of dust-obscured star formation. Larger spectroscopic samples are needed to understand whether the color excess is due exclusively to dust-obscured star formation, as well as the role of environment in triggering it.

1. Introduction

It is now widely accepted that galaxy clusters, the densest associations of matter in the universe, are able to impact the properties of their galaxies. The physical properties of cluster galaxies are found to be starkly different from those of their field counterparts, in terms of colors, star formation activity, morphologies, structural parameters, and ages (e.g., Dressler 1980; Postman & Geller 1984; Dressler et al. 1997; Hashimoto et al. 1998; Lewis et al. 2002; Balogh et al. 2004; Mastropietro et al. 2005; Postman et al. 2005; Von der Linden et al. 2010; Sheen et al. 2017; Song et al. 2017; Vulcani et al. 2010, 2017, 2018; Paccagnella et al. 2016; Webb et al. 2020).

Differences emerge because dense environments are believed to accelerate galaxy evolution, producing more massive systems faster (e.g., De Lucia et al. 2004; Gao et al. 2005; Maulbetsch et al. 2007; Shankar et al. 2013; Papovich et al. 2012; Rudnick et al. 2012; Andreon 2013; Newman et al.

2014; Morishita et al. 2016). The direct role of the cluster environment in driving galaxy evolution through cluster specific effects, however, is still largely unclear. Various physical mechanisms, which are either gravitational or hydrodynamic in nature, are often invoked. While the gravitational interactions mainly culminate in the development of tidal features, the hydrodynamic interactions between the galactic interstellar medium (ISM) and the hot intracluster medium (ICM) may lead to gas removal and eventually quench star formation (see, e.g., Boselli & Gavazzi 2006, for a review).

To complicate the picture, clusters are a very heterogeneous population, spanning a wide range of sizes, densities, and temperatures of the ambient medium, and in different phases of their evolution. Some of them have already collapsed and virialized, while others are still in an assembly phase. There are three main modes of mass accretion onto clusters: the steady infall of matter from the surrounding filamentary large-scale structures, the discrete accretion of group-sized objects, and the extreme event of a major cluster–cluster merger. The last is the most energetic event known in the universe (Markevitch et al. 1998) and results in the violent reassembly of the cluster. Such a dramatic reconfiguration of the cluster results in a rapid change in the environment of its member galaxies. The detailed effect mergers have on galaxies, though, is yet to be fully understood, given the complex nature of cluster mergers and, hence, the difficulty in obtaining a detailed picture of their properties.

A way to improve our understanding of the role of the cluster environment in galaxy evolution is to focus on a specific peculiar system and study in detail its effect on its member galaxies. One of the better-characterized structures at intermediate redshift, a critical epoch during which clusters are in a fast mass-growing phase (a cluster with a mass of $10^{14}\ M_\odot$ doubles its mass between redshift 0.6 and redshift 0; Poggianti et al. 2006) is Abell2744 (hereafter A2744). A2744 (also known as the Pandora cluster and as AC 118; Couch et al. 1984) is an X-ray-luminous, merging cluster at $z = 0.3064$, with a virial mass of $7.4 \times 10^{15}\ M_\odot$ (its mass within 1.3 Mpc is $\sim 2 \times 10^{15}\ M_\odot$; Jauzac et al. 2016) and a velocity dispersion σ_{cl} of $\sim 1500\ km\,s^{-1}$ (Owers et al. 2011). It is in a particularly dynamic state owing to its merging history, and distinct components—both on the plane of the sky and in redshift space—have been identified using the X-ray and optical spectroscopy (Owers et al. 2011): two major substructures, the northern core (NC), and the southern minor remnant core (SMRC) within the cluster, plus a region called the central tidal debris (CTD), which is close in projection to the SMRC but exhibits a velocity close to that of the NC, and a region called the northwestern interloper (NWI), characterized by a cold front to the northeast and an extended region of enhanced X-ray surface brightness to the south (see Figure 17 in Owers et al. 2011 for a visual representation of the different components). This configuration can be explained with a scenario of a post-core-passage major merger (see also Girardi & Mezzetti 2000; Kempner & David 2003; Boschin et al. 2006) in addition to an interloping minor merger, with the CTD being a region stripped from the NC by an interaction and the NWI a structure that fell into the main cluster from the south or southeast, initially traveling roughly north or northwest and passing the main cluster core off-center to the southwest. This complex cluster configuration might explain the significant blue galaxy excess of 2.2 ± 0.3 times that of nearby clusters in the same core

regions (Butcher & Oemler 1984; Couch & Sharples 1987; Owers et al. 2011), as well as a predominance of starburst and post-starburst galaxies (Couch & Sharples 1987).

Given its remarkable features that make it an ideal target to investigate the environmental effects on galaxies, A2744 has recently been the subject of extended campaigns on Very Large Telescope (VLT)/MUSE, which have been used both to better characterize the properties of the cluster as a whole, such as the total mass distribution and its lensing capabilities (Bergmaini et al., submitted), and to study the spatially resolved properties of the galaxy members (Bellhouse et al. 2022; Moretti et al. 2022; Werle et al. 2022) for characterizing the link between the cluster properties and star formation activity in cluster galaxies.

In this paper we exploit JWST/NIRCam observations, combined with VLT/MUSE data, to investigate the properties of the galaxies in A2744, to look for evidence of environmental signatures in galaxies located in different regions of the cluster. We parameterize the environment in many different ways, to be sensitive to a wide range of mechanisms taking place in the cluster. Among the many galaxy properties, we focus on galaxy colors and morphologies, to make the best use of the NIRCam photometry.

After characterizing the overall population of cluster and field galaxies, we focus on the most striking feature uncovered by our study: a population of "red excess" galaxies, i.e., galaxies with normal optical and F115W−F150W colors and an excess of up to 0.8 mag in F200W−F444W over the standard red sequence.

A standard cosmology with $\Omega_m = 0.3$, $\Omega_\Lambda = 0.7$, and $H_0 = 70\ km\ s^{-1}\ Mpc^{-1}$ and a Chabrier (2003) initial mass function (IMF) are adopted.

2. Data Observations and Reduction

2.1. Imaging

We use JWST/NIRCam imaging obtained by the GLASS-JWST program ERS-1324 (Treu et al. 2022b), the UNCOVER[23] program GO-2561 (Bezanson et al. 2022), and the Directors Discretionary Time Program 2756, aimed at following up a supernova discovered in GLASS-JWST NIRISS imaging. Taken together, these surveys provide contiguous coverage over 46.5 arcmin^2 (Paris et al. 2023), thus covering three out of the four components discussed in Section 1.

GLASS-JWST NIRCam observations were taken in parallel to NIRISS observations of A2744 on 2022 June 28–29 and in parallel to NIRSpec observations of the cluster on 2022 November 10. They consist of imaging in seven bands: F090W (total exposure time: 11,520 s), F115W (11,520 s), F150W (6120 s), F200W (5400 s), F277W (5400 s), F356W (6120 s), and F444W (23,400 s). As the primary spectroscopic target was the A2744 cluster, these parallel images are offset to the northwest.

The UNCOVER NIRCam observations were taken on 2022 November 2–15. They target the center of the cluster and the immediate surroundings. These images are composed of four pointings and consist of imaging in seven bands: F115W (10,823 s), F150W (10,823 s), F200W (6700 s), F277W (6700 s), F356W (6700 s), F410M (6700 s), and F444W (8246 s).

---

[23] https://www.stsci.edu/jwst/science-execution/program-information.html?id=2561

Finally, the DDT program 2756 (PI W. Chen) targeted the cluster core on 2022 October 20 and December 6 (UT). The DDT filter set is the same as GLASS-JWST, with the exception of the F090W filter.

In our analysis, we also include new and archival Hubble Space Telescope (HST) imaging. For the GLASS fields, this includes HST/ACS data in F606W (59,530 s), F775W (23,550 s), and F814W (123920 s), taken as part of DDT program GO-17231 (P.I. Treu).

The image reduction and calibration and the methods used to detect sources and measure multiband photometry in all fields closely follow those of Merlin et al. (2022) and are presented by Paris et al. (2023).

Source detection was carried out on the F444W band, while aperture fluxes were computed in the other bands on the point-spread-function-matched images. We use corrected aperture photometry, computed as explained by Merlin et al. (2022) and Paris et al. (2023).

2.2. VLT/MUSE Spectroscopy

We make use of all the available VLT/MUSE spectroscopy in the surroundings of the A2744 cluster. We limit our analysis to the areas covered by MUSE observations, excluding additional spectroscopy available in the surroundings of the cluster to have at our disposal a spectroscopically complete sample of galaxies (see below).

For the cluster central region, we rely on the data from the MUSE Lensing Cluster GTO program (Bacon et al. 2017; Richard et al. 2021). Data consist of a 2×2 mosaic of GTO observations, with a field of view of $\sim 2' \times 2'$ centered on R. A. $= 00:14:20.952$ and decl. $= -30:23:53.88$ covering the region that includes the southern and central structures but excludes the northern core and interloper. Four 1 arcmin^2 quadrants were observed for a total of 3.5, 4, 4, and 5 hr, respectively, and the center of the cluster was observed for an additional 2 hr.

Beyond the cluster central part, we make use of MUSE observations of the GLASS-JWST NIRCam fields obtained on the nights of 2022 July 28 and August 20 through the ESO DDT program 109.24EZ.001 (co-PIs Mason and Vanzella; Prieto-Lyon et al. 2022). The data comprise five pointings (four pointings of which are overlapping with NIRCam imaging, one overlapping only with UNCOVER), each with 1 hr exposure time. The raw data are publicly available on the ESO archive.[24] The reduction, calibration, and source detection methods used for this work are identical to techniques described in previous works (Caminha et al. 2017, 2019). The final catalog is presented in Bergamini et al. (2023b).

3. Galaxy Sample

We select galaxies that are in both the MUSE and NIRCam footprints (Figure 1). This choice allows us to assemble a sample with a high spectroscopic coverage. Indeed, outside the MUSE pointings, spectroscopically confirmed galaxies are quite sparse. Computing the ratio of the number of spectra yielding a redshift to the total number of galaxies in the F115W catalog across the same regions as a function of F115W magnitude, we set our spectroscopic completeness limit at F115W = 22.2 for the external pointing and 23.3 for the central

one (>85% completeness). Throughout the analysis, we will adopt the most conservative value in all regions.

We then separate galaxies based on their global environment: we define as cluster members galaxies lying within $3\sigma_{cl}$ from the cluster redshift and assemble a field comparison sample of galaxies in the redshift range $0.15 < z < 0.287$ and $0.326 < z < 0.55$.[25] The final cluster sample, above the magnitude completeness limit, includes 167 galaxies, field sample 19. Figure 2 shows the redshift distribution for the galaxies in both the cluster and coeval field.

To better quantify the effect of the cluster environment on galaxy properties, we adopt four additional different parameterizations:

1. Clustercentric distance. We measure the distance of each galaxy from the cluster core and scale it by the virial radius. We then separate galaxies into three bins, $r = [0, 0.25, 0.5, 1.2]$ (see Figure 1). Each bin contains 105 (core), 51 (intermediate), and 11 galaxies (outskirts), respectively. This is one of the most traditional ways to investigate the effect of the environment, but given the merging nature of the cluster, this metric might not be effective in capturing environmental effects.

2. Cluster total surface mass density. We use the best-fitting total surface mass density map obtained from an improved version of the strong-lensing model presented in Bergamini et al. (2023a) (see footprint in Figure 1). We refer to Bergamini et al. (2023a) for a more detailed description of the model. For each galaxy, we subtract its total mass contribution from the originally reconstructed total mass map of the cluster and measure the mean values of the total surface mass density in annuli with radii of $1''$ and $2''$ centered around it. We then consider three equally populated bins of surface mass density. The three bins, whose limits are $\log(\Sigma_{mass}[10^{12}M_\odot/\ kpc^2]) = [-3.29, -3.02, -2.78, 1.0]$, contain 57, 54, and 56 galaxies, respectively.

3. Projected local galaxy density. Considering only the spectroscopically confirmed cluster members, above the magnitude completeness limit, for each galaxy we compute the circular area containing the five nearest projected neighbors (A_5). When this circle extends beyond the field of the observations, we take A_5 to be the area of the circle that intersects with the observed field, to correct for edge effects. Local galaxy number densities are then defined as $\Sigma_{5th} = 5/A_5$ in number of galaxies per Mpc^2. We then consider three bins of projected local density, $\log(\Sigma_5 th[Mpc^2]) = [-3.25, -2.5, -2.12, -1.5]$. These thresholds ensure that low-density regions are isolated from the densest one. The different bins contain 25, 71, and 71 galaxies, respectively.

4. Signatures of merger remnants. We select galaxies belonging to the different subcomponents identified by Owers et al. (2011) and discussed in the Introduction (see Figure 1). Three of these regions are covered by our data. SMRC and CTD are cospatial but separated in redshift, as shown in the inset of Figure 2. A total of 46 galaxies belong to the SMRC, 61 to the CTD, and (44) 51 to the

---

[24] http://archive.eso.org/wdb/wdb/eso/sched_rep_arc/query?progid=109.24EZ.001

[25] Note that the implied stellar mass limits can be up to 1.3 dex different for galaxies at the two edges of the field redshift bin. Given the small sample statistics, though, we cannot adopt the most conservative completeness mass limit.
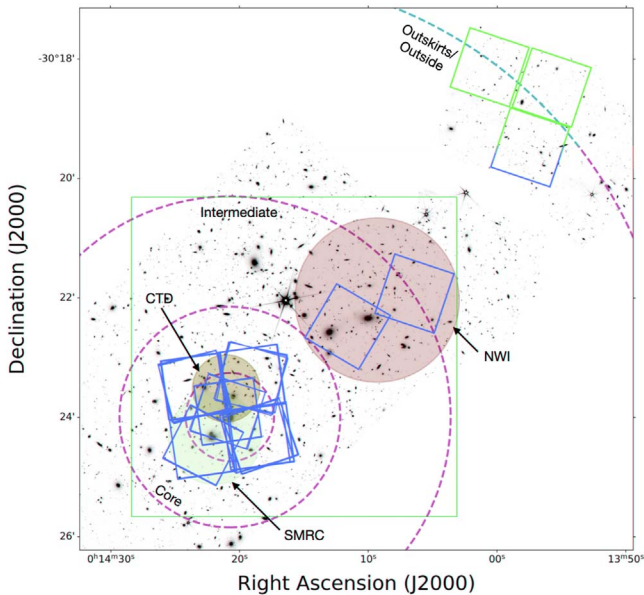
Figure 1. Overview of A2744 showing the NIRCAM F115W image of the cluster, with the MUSE footprint shown by the green squares. Dashed magenta circles indicate regions within $0.1r/r_{200}$, $0.25r/r_{200}$, $0.5r/r_{200}$, and $1r/r_{200}$. Filled circles represent the approximate location of the SMRC (pink), CTD (purple), and NWI (navy), from Owers et al. (2011). SMRC and CTD are actually separated in redshift space, as shown in Figure 2. The red square represents the area over which the total surface mass density of the cluster has been reconstructed by Bergamini et al. (2023a).
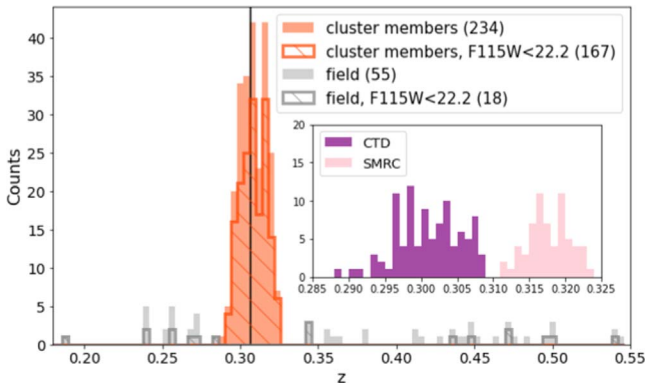
Figure 2. Redshift distribution of the sample. Orange histograms represent cluster members; gray histograms represent the field sample. Filled histograms show the full sample; hatched histograms show galaxies above the magnitude limit. The black vertical line indicates the cluster redshift. The inset shows the redshift distribution of the SMRC and CTD, highlighting the difference in redshift of the components that instead overlap in space.

NWI. A total of 11 galaxies are outside these regions and correspond to the outskirts described in point 1 above.

Figure 3 shows how the different parameterizations of environment are related: while overall an anticorrelation exists between both projected local density/surface mass density and distance, a large scatter dominates the trends, suggesting that each parameterization is sensitive to different conditions in the cluster.[26]

We stress that the uniqueness of our sample relies on the fact that it has a very high (85%) spectroscopic completeness and

---

[26] We note that the gaps in clustercentric distance at $\sim 0.25r/r_{200}$ and between $0.55 < r/r_{200} < 0.85$ do not correspond to real gaps but are due to our sampling, as shown in Figure 1.

can benefit from an unprecedentedly detailed characterization of environment, in addition to JWST/NIRCam observations, although significantly smaller in number than typical literature samples at similar redshift.

4. Galaxy Properties

4.1. Observed and Rest-frame Quantities

Observed magnitudes and colors are described by Paris et al. (2023). Here we use the total fluxes, measured with A-PHOT on the detection image F444W by means of a Kron elliptical aperture (Kron 1980). Total fluxes are obtained in the other bands by normalizing the colors in a given aperture to the F444W total flux.

We obtain rest-frame colors, stellar masses, and attenuation by fitting synthetic stellar templates to the available NIRCam photometry with ZPHOT (Fontana et al. 2000), following the same procedure described in Santini et al. (2023). Briefly, we fix the redshift to the spectroscopic redshift of the galaxy and build the stellar library following the assumptions of Merlin et al. (2021). We adopt Bruzual & Charlot (2003) models, with a Chabrier (2003) IMF, including nebular emission lines according to Castellano et al. (2014) and Schaerer & De Barros (2009). We assume delayed exponentially declining star formation histories (SFH$(t) \propto (t^2/\tau) \cdot \exp(-t/\tau)$) with τ ranging from 0.1 to 7 Gyr. We let the age range from 10 Myr to the age of the universe at each galaxy redshift. Metallicity is allowed to be 0.02, 0.2, and 1 times solar, and dust extinction is assumed to follow a Calzetti et al. (2000) law with $E(B - V)$ varying from 0 to 1.1. We compute 1σ uncertainties on physical properties by retaining for each object the minimum and maximum fitted masses among all the solutions with a probability $P(\chi^2) > 32\%$ of being correct, both fixing the redshift to the best-fit value.

4.2. Galaxy Morphologies

We utilize several quantitative measures of the morphologies, based on multiple broadband filters, to map how morphology varies with wavelength. Following Treu et al. (2022a; Paper XII of this series), for each band, at its original resolution, we derive five largely adopted quantitative morphological statistics. Specifically, we focus on concentration, shape asymmetry, clumpiness (also called smoothness), Gini, and M_{20}. We refer to the original papers (Abraham et al. 2003; Conselice 2003, 2014; Lotz et al. 2004; Pawlik et al. 2016) for a more detailed description of these parameters and to Treu et al. (2022a) for a detailed description on how quantities were measured on NIRCam data. Briefly, the concentration of light (C) measure (Conselice 2003, 2014) is derived from the ratio of the radii that contain 80% and 20% of the total luminosity of a galaxy, giving an indication of the steepness of the light profile of the source. The shape asymmetry (A_S) is derived from the difference between the binary detection mask and the same mask rotated by $180°$ (Pawlik et al. 2016). A_S measures the morphological asymmetry, regardless of the light distribution inside the galaxy. The Gini structural parameter (G) quantifies the degree of inequality of the light distribution in a galaxy (Abraham et al. 2003; Lotz et al. 2004), with lower values indicating a more homogeneous distribution and higher values describing a more concentrated source of flux. M_{20} is defined as the ratio of the second-order moment of the brightest 20% of pixels in a galaxy's image and the second-order
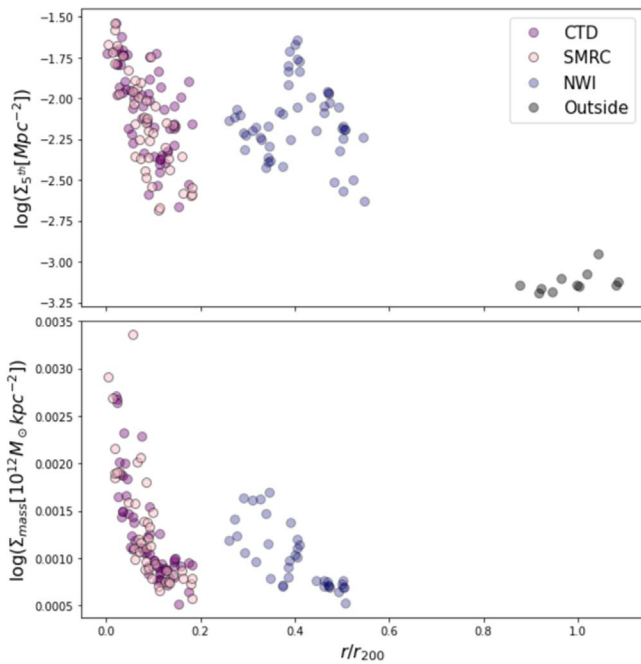
Figure 3. Top: projected local density vs. clustercentric distance. Bottom: projected surface mass density vs. clustercentric distance. Points are color-coded according to the merger remnant signatures, as indicated in the labels.

moment of the entire image (Lotz et al. 2004). This parameter is sensitive to bright features offset from the galaxy center, which makes it suitable for detecting large disturbances in a galaxy's morphology. The clumpiness parameter (cl) quantifies the contribution of small-scale structures in a galaxy (Conselice 2003). A completely smooth light distribution in a galaxy without bright small-scale structures has cl = 0. We derive the clumpiness as in Calabrò et al. (2019), taking the ratio of the flux in the clumpy regions to the total flux of the galaxy.

We adopt the lines used in Lotz et al. (2008) to separate different types of galaxies in Gini, M_{20} space, based on the F814W filter:[27]

1. mergers: $G > -0.14M_{20} + 0.33$.
2. E/S0/Sa: $G \leqslant -0.14M_{20} + 0.33$ and $G > 0.14M_{20} + 0.80$.
3. Sb/Ir: $G \leqslant -0.14M_{20} + 0.33$ and $G \leqslant 0.14M_{20} + 0.80$.

5. Results

To start, we illustrate the visual morphologies of the galaxies as seen at near-IR (NIR) wavelengths, and then we will proceed with a more quantitative analysis of the galaxy colors and morphologies.

Figure 4 presents the projected phase-space (galaxy velocity in the cluster vs. the clustercentric distance) diagram for the galaxies in the cluster. In the case of relaxed clusters, the position of the galaxies in this space can be associated with different times since first falling into the cluster. According to Rhee et al. (2017), four different regions can be identified, where the majority of galaxies lie at a given epoch after they enter in the cluster halo: first (not fallen yet), recent (0 Gyr < t_{infall} < 3.63 Gyr), intermediate (3.63 Gyr < t_{infall} < 6.45 Gyr),

and ancient (6.45 Gyr < t_{infall} < 13.7 Gyr) infallers (see Smith et al. 2015; Pasquali et al. 2019, for other approaches). Obviously, these numbers need to be taken with caution, and galaxies entered at each epoch can be found beyond the corresponding region. As already discussed, A2744 is a complicated structure, and clustercentric distances and relative velocities cannot be used to establish time since infall. Nonetheless, it is interesting to inspect morphologies in this plane, for illustrative purposes. The space in Figure 4 is divided into bins, and an example galaxy, extracted randomly from the ones entering that bin, is shown for each bin to indicate typical morphologies corresponding to that combination of parameters.[28]

A variety of morphologies are evident, and the mix has some dependencies on the position within the plane. Galaxies in the outskirts still present spiral-like morphologies and are all disky, and their morphology seems not to strongly depend on their velocity. Among these ones, it is interesting to note that the position of those with low relative velocities, hence located in the region preferentially occupied by intermediate infallers, supports the idea that these objects have experienced a slow cluster effect for a long time, which has not altered the morphology.

Galaxies located in the region of the recent infallers, hence at rather high relative velocities, generally appear to have a spiral morphology, suggesting that the hostile cluster environment has not had the time yet to affect the galaxy appearance. Among these ones, a few galaxies with very high velocities show asymmetries and signs of ram pressure stripping. Some of them were previously known (Owers et al. 2012; Rawle et al. 2014; Bellhouse et al. 2022; Moretti et al. 2022), while a few are new discoveries. We return to this in Section 6. In contrast, galaxies with lower velocities present less disturbed disks.

Galaxies in the region of the ancient infallers present a wide variety of morphologies, from very elliptical cases (especially at very low clustercentric distances) to disky objects with a well-defined spiral morphology, similarly to what was found by Kelkar et al. (2019), who analyzed 10 clusters between $0.4 < z < 1$. Undisturbed spiral galaxies hence still survive also in a hostile environment such as the core of a merging system.

5.1. Galaxy Colors

The new wavelength range covered by JWST allows us to explore a new set of galaxy colors and unveil trends undetected in the optical regime. Figure 5 shows the observed F115W −F150W, F200W−F356W, and F200W−F444W colors, as a function of NIR magnitude. The first relation has measured scatter of 0.04 mag. This small value is similar to the scatter of the color–magnitude relation of local clusters (e.g., Valentinuzzi et al. 2011). A total of 1.6% of the galaxies lie above 3σ from the relation, and 2.6% lie below. No clear differences seem to emerge between cluster and field galaxies. Considering instead the F200W, F356W, and F444W bands, populations of galaxies with significantly red colors emerge. Fitting the relation and considering galaxies outside the 3σ (=0.16 mag) region, in both cases we find that only one field galaxy has a color bluer than the fitted relation, while 30 galaxies (∼16%) have significantly redder colors than the bulk of the population

---

[27] For galaxies with no F814W coverage we use F606W, having checked that classifications are consistent for galaxies with both bands.

[28] We remind the reader that the observed gaps in clustercentric distance are due to our sampling, as shown in Figure 1.
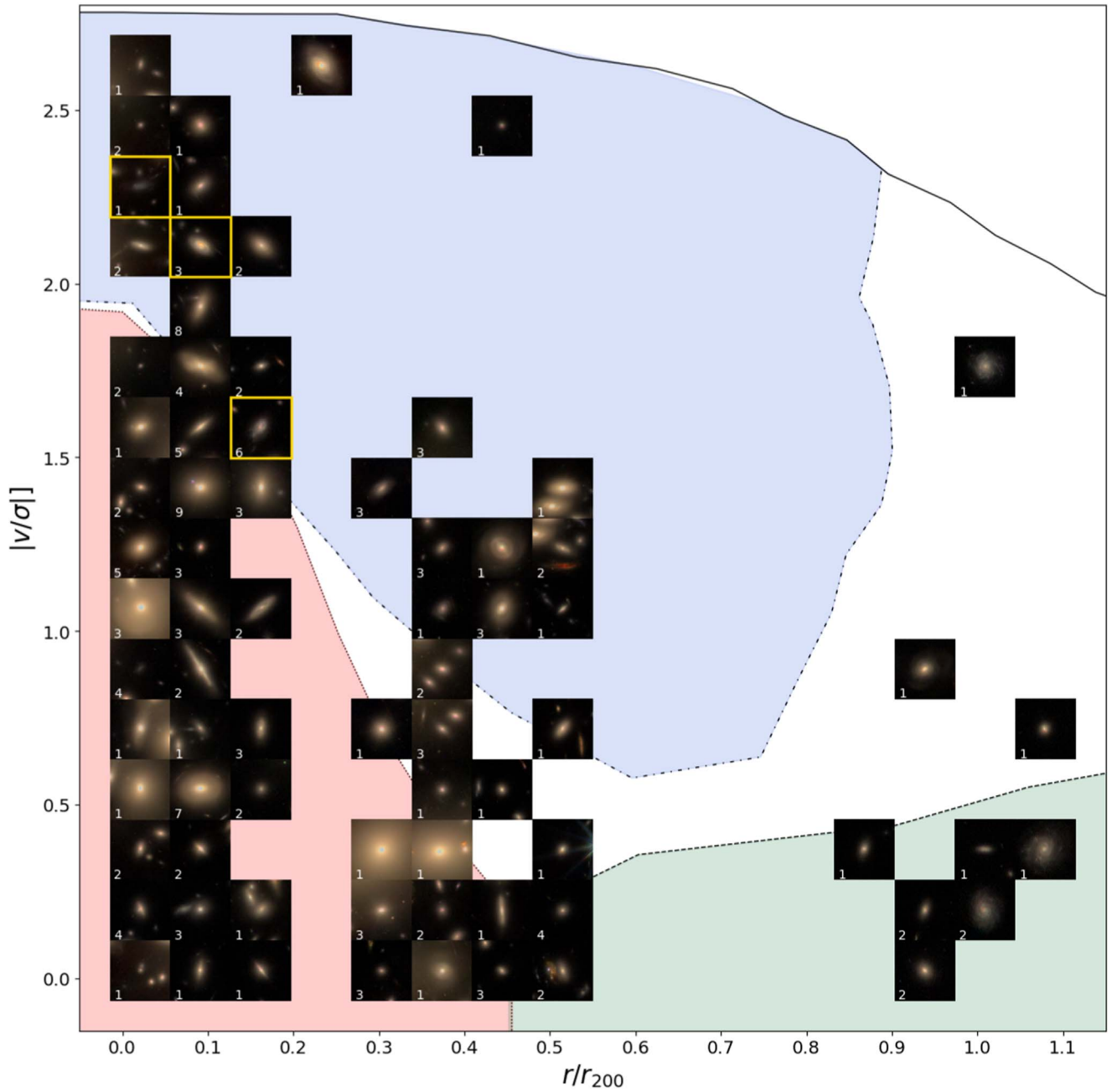
Figure 4. Grid of sample galaxies in the projected phase space. At each location on the grid, an example galaxy is shown in order to visualize the different visual morphologies that occupy different regions of the space. Images are obtained combining the F115W, F150W, and F200W passbands. White numbers indicate the number of galaxies in each bin. Galaxies surrounded by a yellow box are cases of ram pressure stripping (see text for details). The different regions defined by Rhee et al. (2017) are shown with different colors: red = ancient; green = intermediate; blue = recent. The solid black line indicates the limit of subhalos, to define galaxies bounded to the clusters.

in the F200W−F356W color and 32 galaxies (∼17%) in the F200W−F444W colors. In the first case, galaxies can be up to 0.6 mag redder than the best fit; in the second case, up to 0.8 mag. These galaxies include, but are not limited to, the reddest outliers in the F115W−F150W color. Galaxies with normal F115W−F150W colors can be much redder at longer wavelengths. The two populations of galaxies above the best-fit relation overall overlap, even though five galaxies are outliers only in the F200W−F356W color and seven only in the F200W−F444W color. The exact overlap, though, is very sensitive to the threshold adopted to select them. From now on, we will call "red excess" the outlier galaxies in F200W

−F444W, the set of bands where deviations are the largest. In Section 6 we will characterize this population in more detail.

We proceed by investigating the variation of galaxy colors with environment. To quantify trends, for each galaxy we measure the difference between the observed color and the value derived from the fit given the galaxy magnitude. Figure 6 plots the distribution of such differences, considering the different parameterizations of environment discussed in Section 3.

When considering the F115W−F150W color, no differences emerge either between the field and cluster or between cluster galaxies in different finer environments. A Kolmogorov–
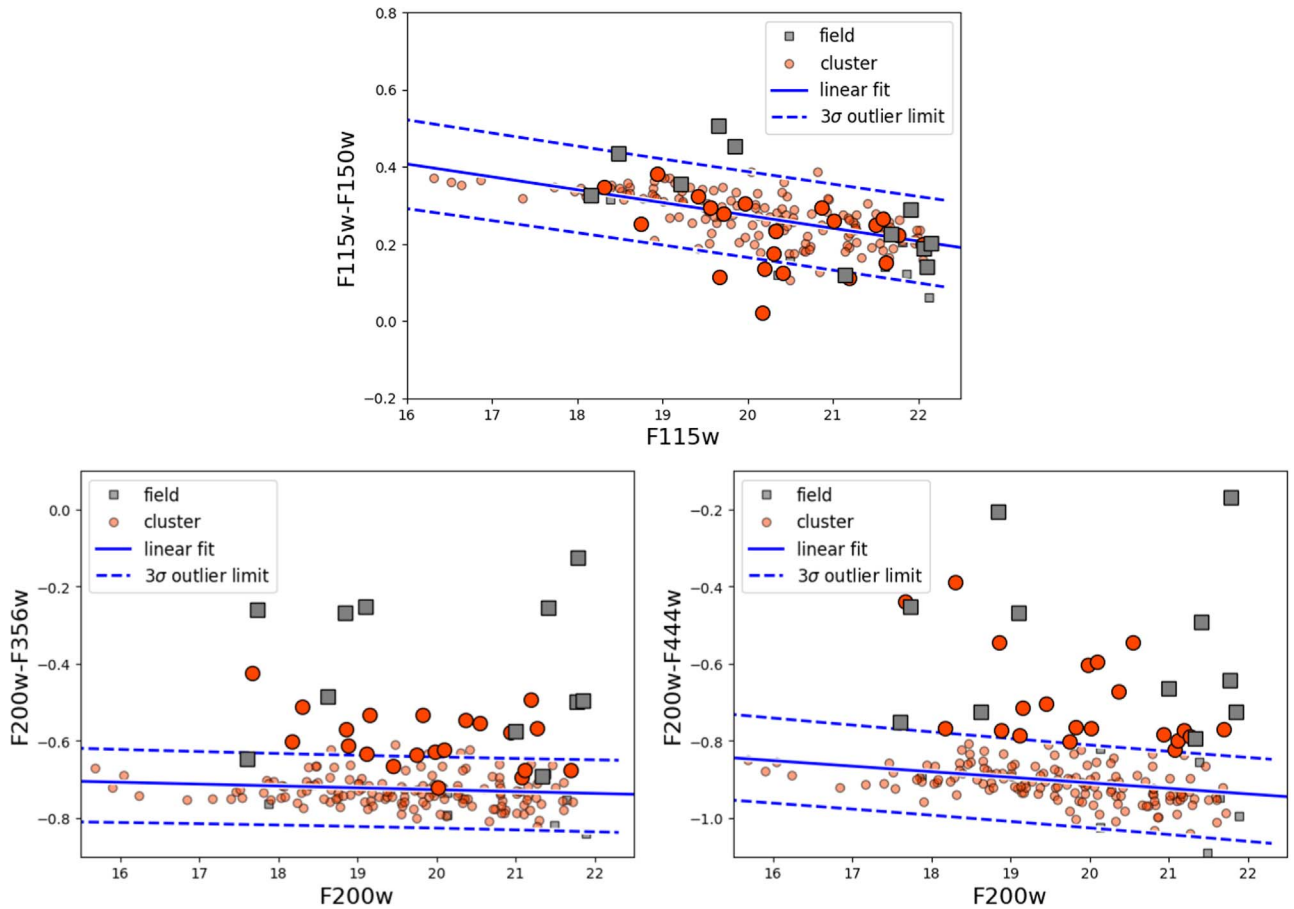
Figure 5. Observed color–magnitude diagram. Top: F115W−F150W vs. F115W. Bottom right: F200W−F356W vs. F200W. Bottom left: F200W−F444W vs. F200W. Red circles: cluster galaxies; gray squares: field galaxies. The blue solid line represents the best fit of the relation, obtained with an iterative 3σ clipping procedure. The dashed line shows the 3σ error. Galaxies deviating more than 3σ from the best fit in the F200W−F444W vs. F200W plane are indicated with larger symbols in all panels.

Smirnov (K-S) test run pairwise on the different samples never rejects the null hypothesis that samples are drawn from the same distribution with high significance ($P_{\mathrm{val}} > 0.2$). The only difference is that the field is characterized by large scatter in color, much larger (by about 3 times) than any of the other samples. Considering the finer definitions of environments, no significant differences emerge, and distributions are rather peaked.

When considering the F200W−F356W color, the field is significantly different from other samples, and the K-S test always supports this statement. No significant other differences emerge when inspecting the other samples.

Considering instead F200W−F444W colors, the distributions are much more widely spread, and hints of environmental effects emerge. The field distribution is characterized by an even larger scatter than in F115W−F150W, and the K-S test finds significant differences ($P_{\mathrm{val}} < 10^{-5}$) when the field is compared to all samples, except for the outskirts (which correspond to the outside when using the signature of merging remnants) and low-density regions. The field median value is almost 0.2 mag redder than the core/high-density regions, and median values are statistically different ($>2\sigma$) even though the large scatter prevents us from drawing solid conclusions. The field is much like the outskirts/outside: despite the small number statistics, distributions are peaked at the same value, and the K-S test establishes with high significance ($P_{\mathrm{val}} < 0.02$) that the outskirts/outside are different from both the core and

intermediate regions. In contrast, galaxies within $0.5r_{200}$ have a rather peaked distribution centered around 0, and no differences emerge between the two populations. No additional significant differences emerge using the other parameterizations of environment, even though redder galaxies tend to lie at low values of projected local density. The K-S test confirms a different parent distribution for galaxies in the lowest-density bin compared to the other two bins.

5.1.1. Quiescent Fractions in the Different Environments

In addition to observed colors, we next inspect rest-frame colors. Figure 7 shows the rest-frame $U - V$ versus $V - J$ color diagrams for galaxies in the different environments. Star-forming and quiescent galaxies have been shown to exhibit a bimodality in this plane out to $z \sim 3$ (Labbé et al. 2005; Williams et al. 2009; Whitaker et al. 2011; Muzzin et al. 2013; Straatman et al. 2014, 2016). As expected, the sequence of quiescent galaxies is well visible. The fraction of quiescent galaxies strongly depends on the environment: in the cluster cores it is maximum ($90\% \pm 3\%$), while in the field it is minimum ($20\% \pm 10\%$). Considering cluster outskirts, the fraction of quiescent galaxies is comparable to that of the field, suggesting that the star formation activity is not significantly affected at the virial radius, in agreement with a vast body of literature. At $0.5r_{200}$ the fraction of quiescent galaxies is intermediate between the core and the outskirts. Considering
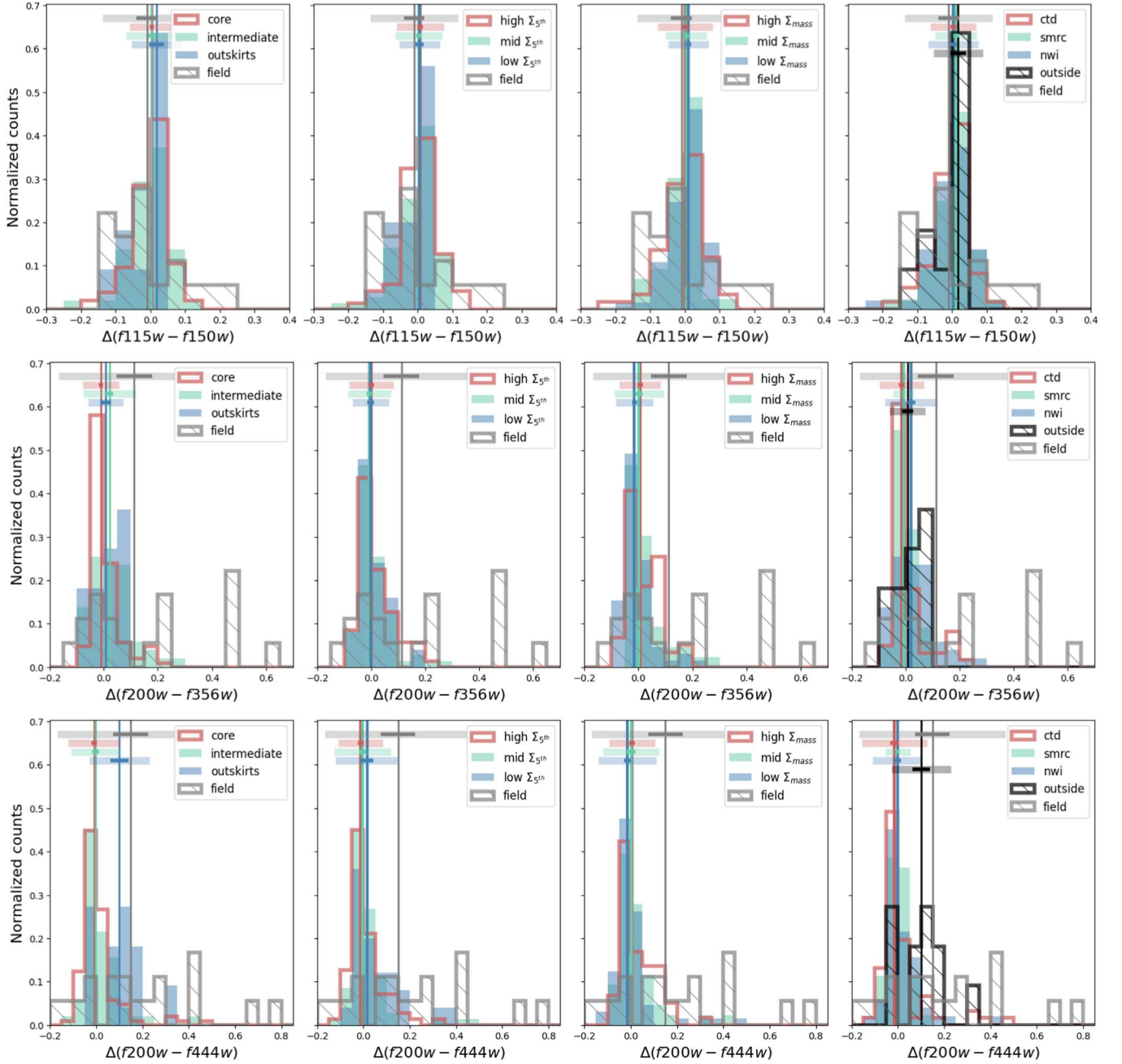
Figure 6. Distributions of the differences between the galaxy color and their expected value according to the fit to the entire sample, shown in Figure 5, given their magnitude. Top panels show the F115W−F150W color distribution; middle panels, F200W−F356W; and bottom panels, F200W−F444W. From left to right, different parameterizations of environment are considered: clustercentric distance, projected local density, surface mass density, and signatures of merger remnants. Colors refer to the different subsamples, as indicated in the legend. Vertical lines show median values; thick horizontal lines show the standard error of the distribution ($1.253 \times \sigma$; lighter lines) and the error on the median ($1.253 \times \sigma / \sqrt{n}$ with n number of galaxies; darker lines).

the projected local density, the fraction of quiescent galaxies increases from the lowest- to the highest-density bins, while no statistically significant differences are observed when considering the surface mass density. We remind the reader, though, that the surface mass density measurements are limited to the central part of the cluster, so the mass range spanned is much smaller than the density range probed. Considering the merger remnant signature, the fraction of quiescent galaxies is systematically higher in the CTD (∼85%), SMRC (∼98%)— which corresponds to the cluster core—and NWI (∼82%) than in the regions outside any merger remnant. It appears evident that past mergers have induced a higher fraction of passive

galaxies. We will discuss the position of the red excess galaxies in this plot in Section 6.

Finally, we also look for trends in colors considering galaxies in the different regions of the projected phase space, but no significant differences emerge in their mean values and scatter.

To summarize, quiescent fractions based on rest-frame optical−NIR color strongly depend on environment, whichever definition is adopted. Considering observed colors, JWST unveils a population of extremely red objects, with normal optical colors, whose origin might be linked to the environment.
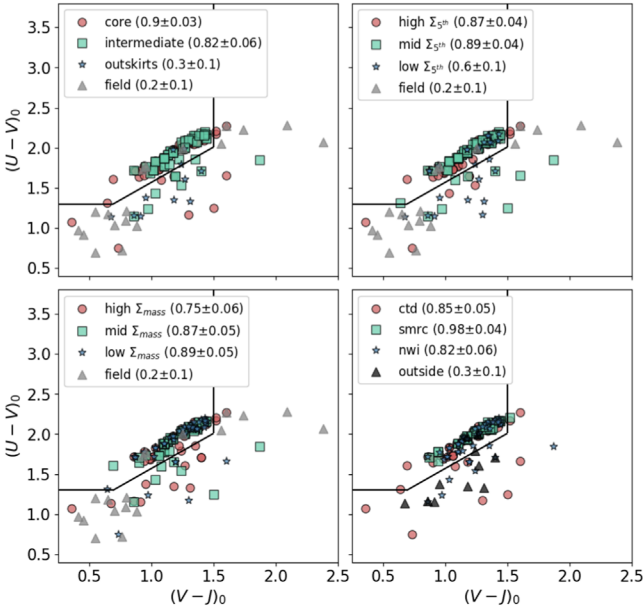
Figure 7. Rest-frame $U - V$ vs. $V - J$ diagram of galaxies in the different environments. Top left: clustercentric distance. Top right: projected local density. Bottom left: surface mass density. Bottom right: signatures of merger remnants. The separation between star-forming and quiescent galaxies is from Williams et al. (2009). Colors refers to the different subsamples, as indicated in the legend. In the legend, fractions of quiescent galaxies are reported.

We note that, given our small sample size, we cannot isolate the role of stellar mass in affecting quiescent fractions, which is known to play an important role in galaxy evolution (see, e.g., Peng et al. 2010; Vulcani et al. 2011; Ilbert et al. 2013). For similar reasons, we will neglect the role of stellar mass also in what follows.

5.2. Galaxy Morphologies

We now investigate how the morphological parameters change across wavelength, considering both HST and JWST bands, hence covering the rest frame 0.3–3.5 μm at the redshift of the cluster. We consider the Gini, M_{20}, concentration, clumpiness, and shape asymmetry parameters, and for each index we measure the difference between the value in a given band and the value measured in the F444W, called Δindex. Figure 8 shows how the Δindex varies as a function of rest-frame wavelength. To increase the statistics, we here consider field and cluster galaxies together, having checked that there are no significant environmental dependencies. Data distributions are shown in terms of violin plots, which give the probability density of the data at different values, smoothed by a kernel density estimator. To summarize the distributions in each band, we also compute the median value of the Δindex in each band, along with the first and third interquartiles of its distribution.

While, within uncertainties and scatter, morphological indexes do not vary dramatically as a function of wavelength across the entire dynamic range probed by these observations, some trends emerge. The Gini parameter is the smallest when measured at the bluest wavelengths (from HST), but then it is consistent with the values measured in the F444W from $\lambda_{rf} > 0.5$ μm. $\Delta(M_{20})$ is consistent with 0 for $\lambda_{rf} < 0.7$ μm, but then it is <0 between 1 and 2.5 μm. F356W measurements are again compatible with those measured in F444W. Concentration is systematically larger than in F444W when measured at

$\lambda_{rf} < 2$ μm, while no deviations are visible in the clumpiness. As far as shape asymmetry is concerned, there are hints of a larger asymmetry in the bluest bands and a smaller one in the central one, but larger samples will be needed to confirm such trends.

These results are consistent with the fact that galaxies can appear substantially different at shorter wavelengths than at longer ones (e.g., Bohlin et al. 1991; Kuchinski et al. 2000; Windhorst et al. 2002). This shows how little morphology changes at $\lambda_{rf} > 1$ μm. Indeed, the optical band light is a mix of warm and cool stellar components, in which older populations have significant influence. In optical images of spiral galaxies, both the cool bulge and hot spiral arm components can be bright. In contrast, NIR light emphasizes cool stellar components, mainly the red giant branch or cool supergiants, while simultaneously reducing the effects of extinction from dust. Spiral structures are often much less prominent (Elmegreen & Elmegreen 1981).

5.2.1. The Morphological Mix in the Different Environments

Next, using the combination of Gini and M_{20} as discussed in Section 3, we obtain an estimate of galaxy morphology. In the cluster, 98 galaxies (0.60 ± 0.03) are classified as E/S0/Sa, 61 (0.38 ± 0.04) as Sb/Irr, and 3 (0.02 ± 0.01) as merger. In the field, the number of E/S0/Sa is 5 (0.3 ± 0.1), the number of Sb/Irr is 12 (0.7 ± 0.1), and the number of mergers is 0. In agreement with previous results (e.g., Dressler 1980; Calvi et al. 2012; Fasano et al. 2015; Vulcani et al. 2023), the effect of the environment is clearly visible on the morphological mix. To better quantify where in the cluster galaxies of different morphologies are preferentially located, Figure 9 shows the morphology−environment relations, using the four different parameterizations of environment.

Overall, E/S0/Sa galaxies dominate at all projected local densities and surface mass densities and regardless of merger remnant signatures. They are as common as Sb/Irr only at the lowest densities and outside any merger remnant structure. Only at the lowest surface mass densities do Sb/Irr galaxies dominate. Considering clustercentric distance, the fraction of E/S0/Sa decreases from the core to the intermediate regions, where the incidence of E/S0/Sa and Sb/Irr is similar.

6. An F200W−F444W "Red Excess" Population

Figure 5 has unveiled an unexpected population of "red excess" galaxies, visible only when the reddest JWST bands are considered.

First of all, to test the reliability of the adopted photometry (Paris et al. 2023), we perform the same analysis discussed in Section 5.1, using instead the photometry obtained by Weaver et al. (2023) in the context of UNCOVER, based on completely independent reduction and extraction algorithms. A total of 21/32 galaxies are identified also with the alternative photometry, reassuring us about the reliability of the population. Of the remaining galaxies, 4 have F115W magnitude fainter than our adopted limit of 22.2, according to the Weaver et al. (2023) photometry, 3 have a point-like source that might be affecting the photometry, and 3 are on the cluster main sequence according to the UNCOVER photometry. In contrast, five additional galaxies are "red excess" galaxies according to the UNCOVER photometry; one of these is on our red sequence, and the others are not in our catalog.
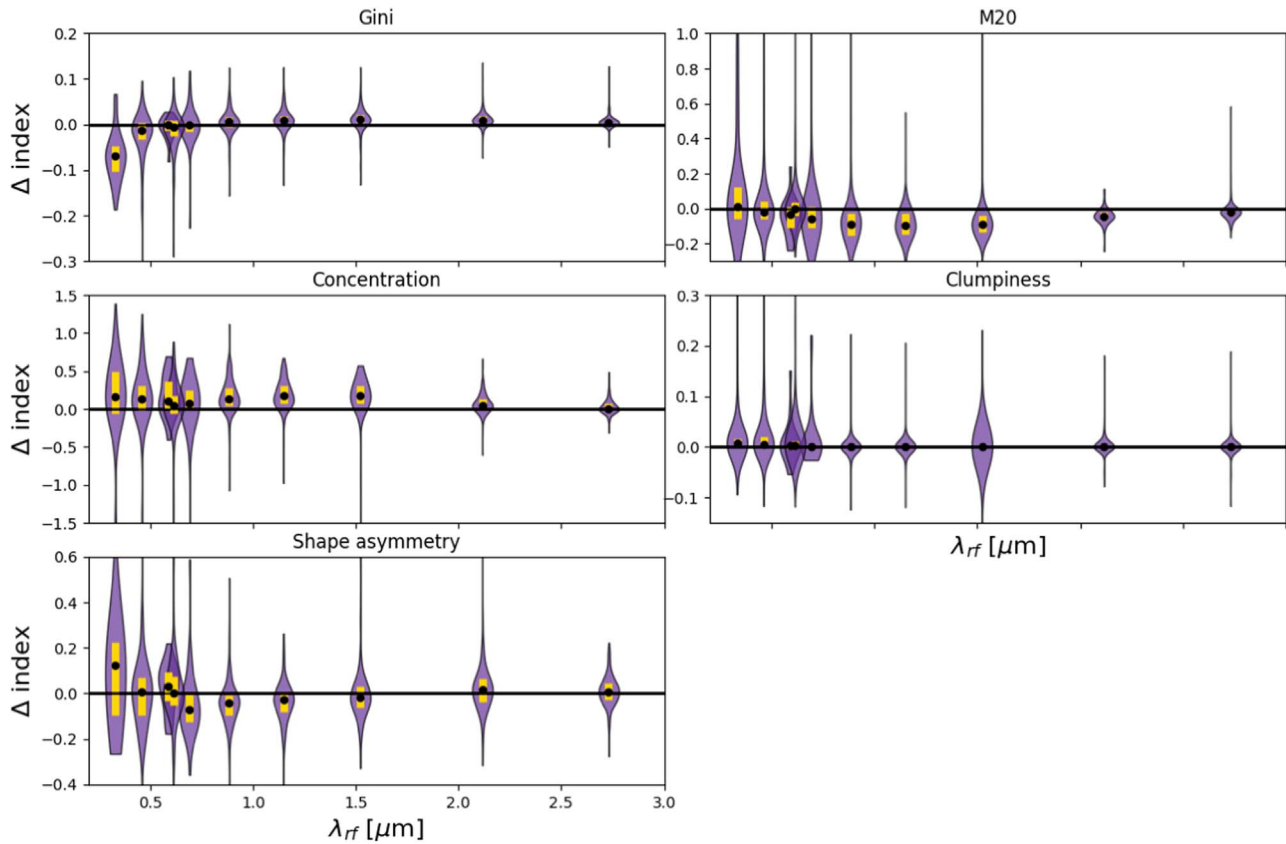
Figure 8. Violin plot distribution of Δindex (= index—index$_{\mathrm{F444W}}$) for five morphological parameters as a function of rest-frame wavelength. All galaxies in the sample, regardless of environment, have been considered. Black points represent median values; gold bars represent the first and third interquartile range. The horizontal black line shows the zero value, which corresponds to no offset.

We now investigate this population in more detail, to understand its origin. In total, 32 galaxies are identified as outliers, constituting $17\% \pm 2\%$ of the analyzed (cluster+field) population. Table 1 summarizes the main properties of the population.

We now characterize various aspects of this population, to shed further light on its origin.

6.1. The Environment of the Red Excess Galaxies

In Figure 6 we showed that the observed F200W−F444W color of the red excess galaxies, or red outliers, might be related to the environment, suggesting that the galaxy surroundings might play a role in triggering the observed features.

A total of 21/32 of the red outliers are in the cluster ($13\% \pm 2\%$ of the cluster population), while 11 are in the field ($55\% \pm 10\%$ of the field population). Figure 10 shows the location of the galaxies within the cluster. Half of the population in the outskirts and about one-third of galaxies in the low-density region have been flagged as red outliers. In such environmental conditions, we typically do not expect to observe strong ram pressure stripping (Jaffé et al. 2018; Gullieuszik et al. 2020), but galaxy−galaxy interaction and past minor mergers can occur (Mihos & Hernquist 1996). The rest of the red outlier cluster sample is located near the cluster core but tends to avoid the densest cluster regions, and many of them have relatively high velocity. They are in the best position for feeling ram pressure stripping (e.g., Jaffé et al. 2018). Indeed, some of these galaxies were already identified as potential ram pressure stripping candidates (Owers et al. 2012;

Rawle et al. 2014). Three of these galaxies have already been confirmed to be ram-pressure-stripped galaxies in Moretti et al. (2022) and Bellhouse et al. (2022) (A2744_06, A2744_09, A2744_10 in their papers, corresponding to our 40243, 41259, 41908). Two other galaxies are outside the area investigated by those papers, and two of them were excluded from their analysis owing to their red color. Of the other galaxies, three (713, 70006036, and 70003981) show signs of stripping, while the others show undisturbed morphology. We discuss morphologies more in detail in the next section.

6.2. Galaxy Morphologies

A total of $63\% \pm 10\%$ of the red outliers are Sb/Irr. They hence are $26\% \pm 5\%$ of the entire Sb/Irr population of the sample analyzed in this work. E/S0/Sa red outliers are only $10\% \pm 3\%$ of the total E/S0/Sa population.

Considering the various indicators of galaxy morphology, red outliers have higher values of shape asymmetry and M_{20}: the median value of A_S for the red outliers is 0.094 ± 0.009, while for the normal (cluster+field) population it is 0.075 ± 0.004; a K-S test rejects with high confidence ($P_{\mathrm{val}} = 0.002$) the hypothesis that samples are drawn from the same parent distribution. The median value of M_{20} for the red outliers is -1.98 ± 0.02, while for the normal (cluster+field) population it is -1.90 ± 0.005; the K-S test shows that this difference is only marginally significant. No differences are detected when comparing median values and distributions of the other parameters. Red outliers hence tend to be more asymmetric and have more bright off-center features with
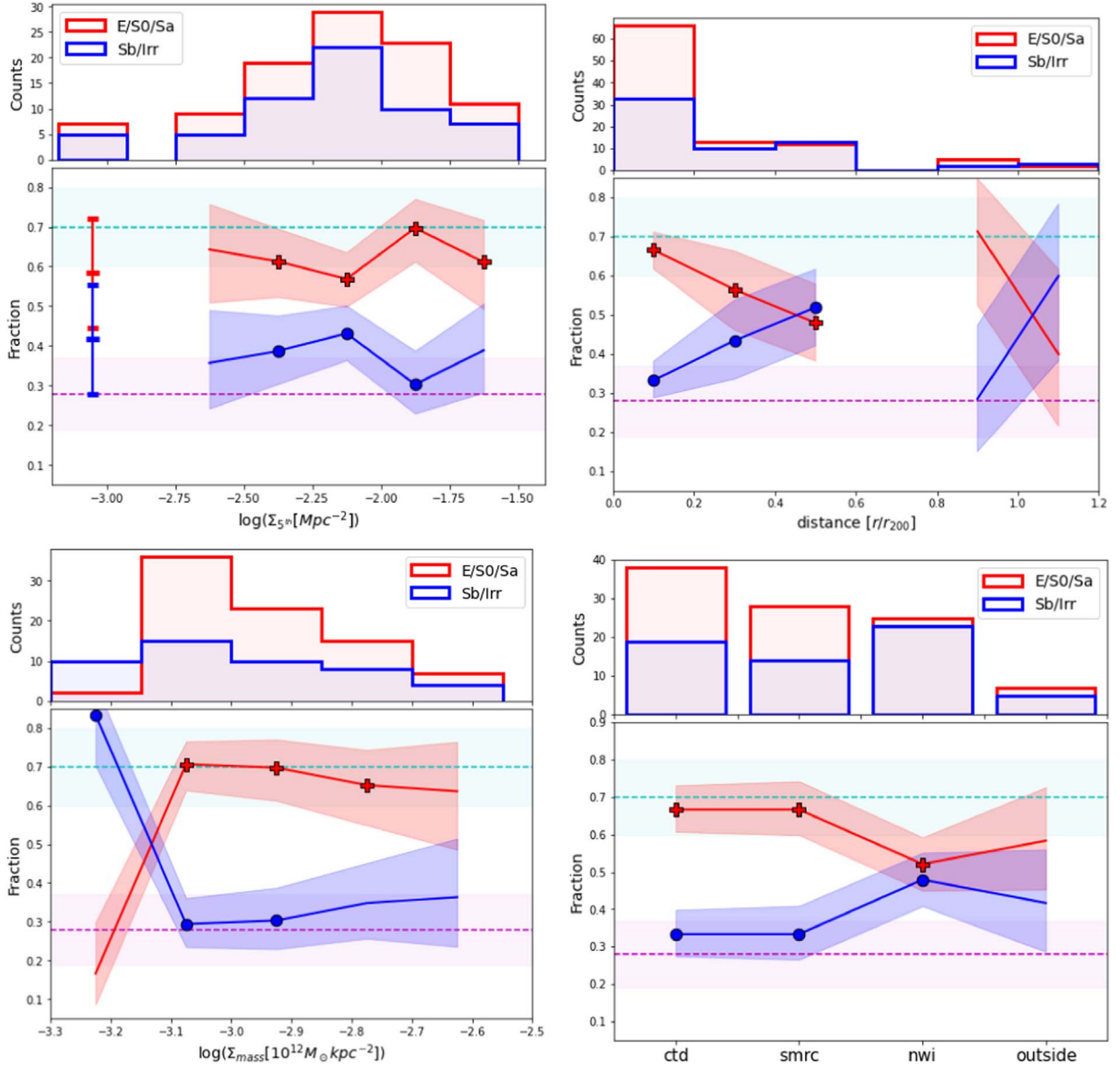
Figure 9. Morphological fractions as a function of the different characterizations of environment. Each quadrant shows a different parameterization: clustercentric distance (top left), projected local density (top right), surface mass density (bottom left), and signatures of past merger (bottom right). In each quadrant, the top panel shows the distribution of galaxies as a function of environment, and the bottom panel shows the morphological fraction. Red crosses and lines and blue circles and lines represent E/S0/Sa and Sb/Irr, respectively. Symbols are plotted only for bins with at least 10 galaxies. Shaded areas represent uncertainties, computed as binomial errors. Horizontal lines refer to values and errors measured in the coeval field (cyan for Sb/Irr, magenta for E/S0/Sa).

respect to the normal population. Disturbances in morphologies must be due to different physical mechanisms in the different environments, as in the field merger and interactions might be responsible for the observed morphology, while in clusters we suggest hydrodynamical mechanisms, as already mentioned.

To better visualize galaxy morphologies, Figure 11 shows the color-composite images for a subset of the red outlier galaxies and the corresponding F200W−F444W color map. A variety of different morphologies emerge, including smooth to clumpy light distributions, well-defined spiral arms, and disturbed galaxies. Many galaxies show asymmetries; some of them show signs of unwinding arms, similar to what is observed in local cluster galaxies (Bellhouse et al. 2021; Vulcani et al. 2022).

The reported cluster galaxies are the four already-known ram-pressure-stripped objects (Owers et al. 2012; Rawle et al. 2014; Moretti et al. 2022) and one of the newly discovered

cases. The color map shows that red color excesses are spread throughout the galaxy disks and, when spiral arms are present, they follow them quite accurately. In 41908, the side of the galaxy corresponding to the galaxy tail to the southwest is much redder than the other side.

Also in the field the color excess tightly follows the spiral arms in the undisturbed galaxy (40508). 70005598 is most likely a case of an interacting galaxy, and a strong gradient in red color excess is observed from north to south, suggesting an environmental influence on this map. In 70004621 and 70005691, two cases of rather small, smooth galaxies, the color excess is also quite smooth.

6.3. Rest-frame Properties

We can use the output from the spectral energy distribution (SED) fitting (Section 4.1) to further characterize the
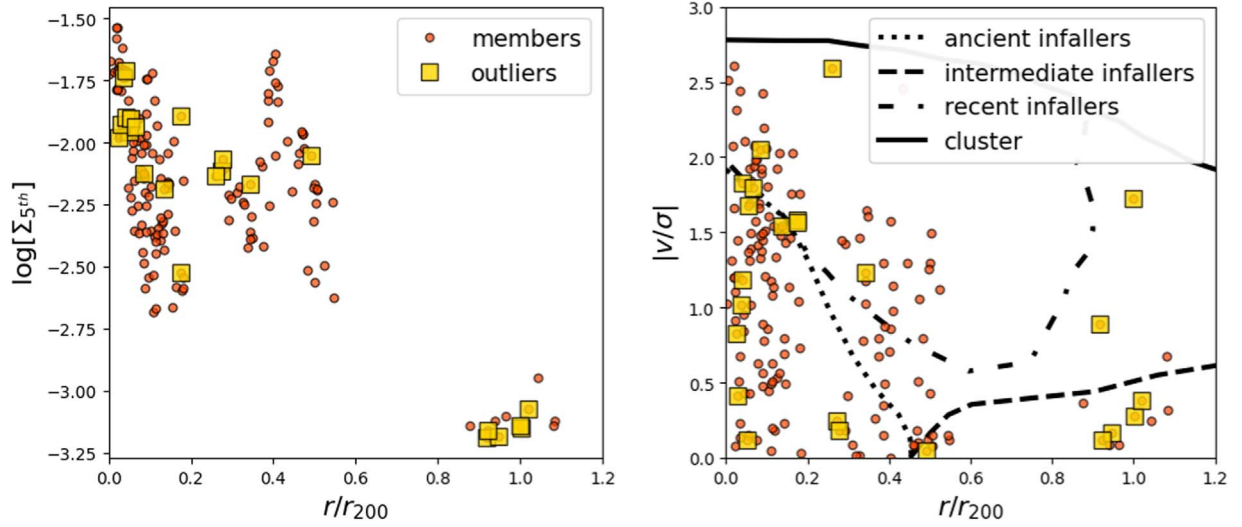
Figure 10. Left: projected local density as a function of clustercentric distance for the cluster population (red circles) and outliers (gold squares). Right: projected phase-space diagram for the same two populations. Lines are as in Figure 4.

Table 1
Properties of the Subsample of Galaxies with the F200W−F444W Excess

ID	RA2000 (J2000)	DEC2000 (J2000)	z	F_f200W (10^{-6} Jy)	F_f444W (10^{-6} Jy)	Env	Dist r/r_{200}
70003396	00:13:55.75	−30:19:54.8	0.3122	60.38 ± 0.03	31.62 ± 0.02	C	0.92
70006036	00:13:56.52	−30:18:45.9	0.3082	35.84 ± 0.04	17.69 ± 0.05	C	1.0
70004788	00:13:57.13	−30:19:13.2	0.3075	13.54 ± 0.01	6.34 ± 0.01	C	0.95
70004550	00:13:57.27	−30:19:27.6	0.3072	13.0 ± 0.01	6.22 ± 0.02	C	0.92
70003713	00:13:59.92	−30:17:58.3	0.3089	7.61 ± 0.02	3.74 ± 0.02	C	1.02
70003666	00:14:01.24	−30:17:57.3	0.3177	36.94 ± 0.03	21.21 ± 0.04	C	1.0
70001043	00:14:07.04	−30:21:53.3	0.3067	25.9 ± 0.02	13.98 ± 0.02	C	0.49
70003476	00:14:11.62	−30:22:24.5	0.2984	42.85 ± 0.07	21.2 ± 0.03	C	0.34
70006666	00:14:13.71	−30:22:40.2	0.308	101.9 ± 0.05	49.98 ± 0.03	C	0.27
70003777	00:14:14.08	−30:22:33.1	0.3052	12.18 ± 0.02	5.98 ± 0.02	C	0.28
70003981	00:14:14.38	−30:22:40.0	0.3234	309.56 ± 0.07	206.65 ± 0.09	C	0.26
713	00:14:16.63	−30:23:03.3	0.2961	33.08 ± 0.03	19.11 ± 0.04	C	0.18
36843	00:14:18.98	−30:24:00.3	0.3056	15.44 ± 0.02	7.5 ± 0.03	C	0.05
40243	00:14:19.43	−30:23:26.9	0.2931	104.46 ± 0.03	63.31 ± 0.03	C	0.08
36211	00:14:20.14	−30:24:07.3	0.301	11.27 ± 0.04	5.45 ± 0.02	C	0.02
35908	00:14:20.41	−30:24:11.9	0.3037	196.12 ± 0.1	96.82 ± 0.09	C	0.03
35693	00:14:20.89	−30:24:17.8	0.2987	82.31 ± 0.04	39.9 ± 0.03	C	0.04
35576	00:14:21.11	−30:24:15.3	0.2998	79.18 ± 0.07	41.04 ± 0.04	C	0.04
34439	00:14:21.67	−30:24:26.6	0.3182	46.07 ± 0.03	22.03 ± 0.03	C	0.07
41259	00:14:22.39	−30:23:03.8	0.2964	174.34 ± 0.04	121.89 ± 0.03	C	0.14
41908	00:14:25.06	−30:23:05.9	0.2962	22.07 ± 0.01	13.37 ± 0.02	C	0.18
70005598	00:13:53.08	−30:18:07.7	0.4378	7.13 ± 0.01	3.95 ± 0.03	F	
70003440	00:13:56.37	−30:19:47.2	0.4494	128.96 ± 0.04	66.13 ± 0.02	F	
70004621	00:13:56.90	−30:19:29.2	0.5414	9.96 ± 0.01	6.33 ± 0.01	F	
70005765	00:13:59.29	−30:19:18.8	0.3432	105.58 ± 0.05	87.28 ± 0.04	F	
70005157	00:13:59.32	−30:19:07.7	0.343	14.5 ± 0.03	7.86 ± 0.03	F	
70005691	00:13:59.42	−30:19:14.3	0.3431	10.6 ± 0.03	5.1 ± 0.03	F	
70004342	00:14:10.29	−30:22:55.7	0.4734	6.99 ± 0.01	5.98 ± 0.03	F	
41371	00:14:17.53	−30:23:07.1	0.4988	83.02 ± 0.04	53.98 ± 0.05	F	
37672	00:14:21.58	−30:23:51.4	0.474	6.6 ± 0.02	3.39 ± 0.01	F	
37257	00:14:21.68	−30:24:01.4	0.4971	292.16 ± 0.05	192.52 ± 0.05	F	
40508	00:14:24.01	−30:23:23.0	0.19	328.73 ± 0.04	164.78 ± 0.05	F	

population. Figure 12 shows the location of the red outliers and of the normal population in the rest-frame $B − V$ color versus stellar mass plane, in the UVJ diagram, and in the star formation rate (SFR) versus mass plane. It also shows the

stellar mass and $E(B − V)$ distributions of the different populations.

Red outliers span a wide range in galaxy colors and stellar mass. A total of 20/32 galaxies lie below the red sequence,
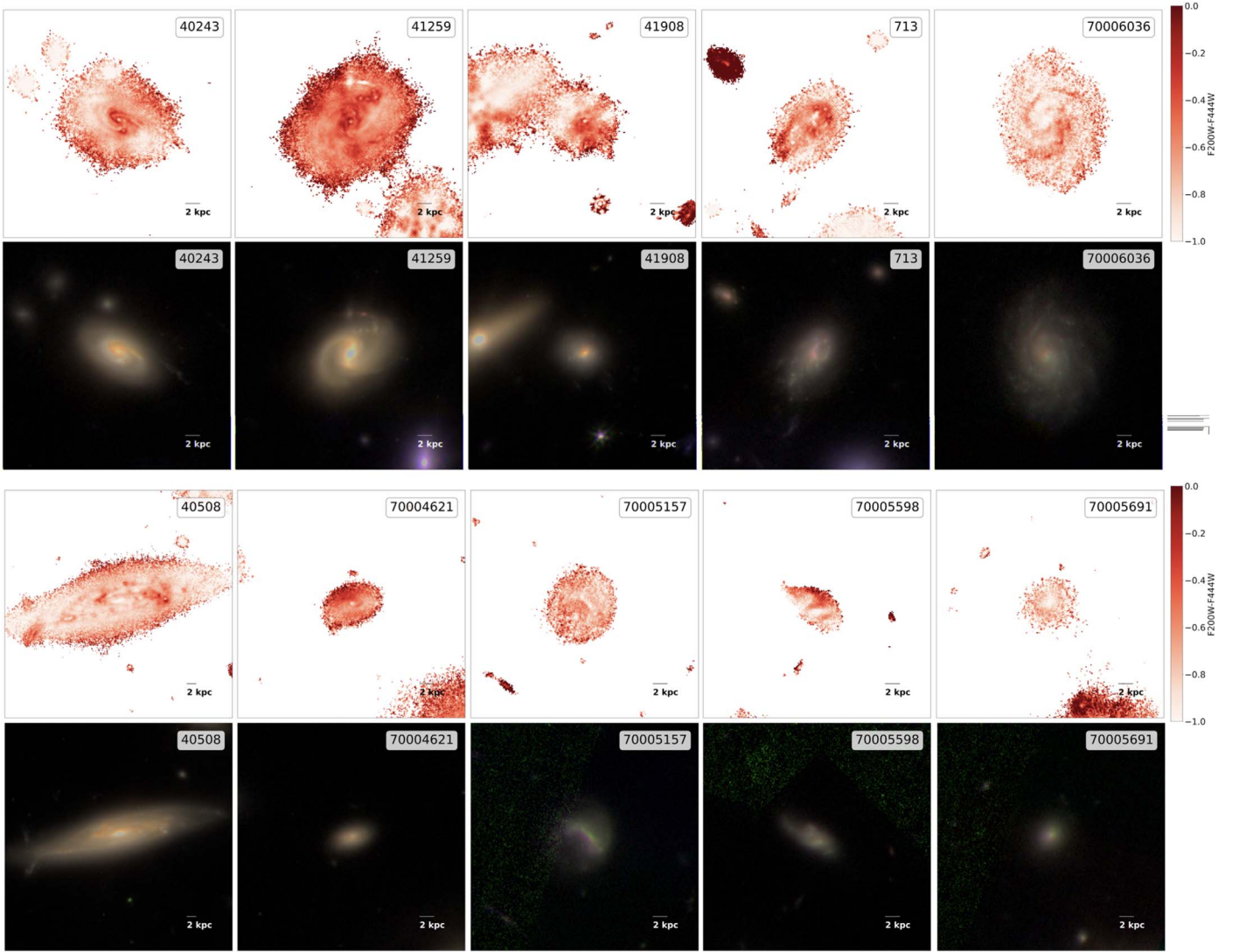
Figure 11. F200W−F444W maps and corresponding color-composite (F115W+F150W+F200W) images of a subset of the extremely red population identified in Figure 5. The top rows shows galaxies in the cluster; the bottom row shows galaxies in the field. The physical scale is reported in the lower right corners.

defined fitting the entire cluster relation adopting a 3σ clipping method. Eleven lie on the main sequence, and only one above. Therefore, not all of them are clearly star-forming. This is confirmed by the analysis of the *U, V, J* colors: according to the *UVJ* diagram, $34\% \pm 8\%$ of the outliers are quiescent. A similar value ($29\% \pm 8\%$) is obtained when using a cut in specific SFR (sSFR) to separate star-forming and quiescent galaxies (sSFR $> 10^{-11.5}$ yr^{-1}). Five of the 11 quiescent red outliers might include a point-like source; four of them have a companion. This population should then be taken with caution. Overall, red outliers represent $50.0\% \pm 0.7\%$ of the entire (cluster+field) star-forming population. Considering the star-forming galaxies with late-type morphology in the cluster core, six out of seven are considered red outliers.

In the cluster, red outliers are typically less massive than their normal counterparts: the median stellar mass value of the nonoutlier cluster population is $\log M_*/M_\odot = 10.08 \pm 0.05$, and that of the cluster outliers is $\log M_*/M_\odot = 9.9 \pm 0.1$. A K-S test rejects the null hypothesis that the two samples are drawn from the same parent distribution with high confidence ($P_{\rm val} = 0.003$). No differences are found in the field, most likely due to the small sample size.

The red outliers span a wide range in star-forming properties: using the SFR estimated from the SED fitting, the bottom left panel of Figure 12 shows that while some red outliers are just above the sSFR threshold adopted to separate star-forming from quiescent objects, many others can reach SFRs of 100 $M_\odot$ yr^{-1}. The sample is too small to obtain robust fits to the relation, but clear differences between red outliers and normal galaxies are evident. For reference, we report the fit to the SFR −mass relation obtained by Santini et al. (2009) in the redshift range $0.3 < z < 0.6$, converted to our adopted IMF. The work of Santini et al. (2009) is also based on SED fitting, and they used the same code as the one adopted in this work. We note, though, that the quality of the data, the redshift range, and methodologies are different, so results cannot be directly compared.

Red outliers also have systematically higher values of $E(B-V)$ than normal galaxies (bottom right panel of Figure 12): the mean $E(B-V)$ of the red outliers is 0.19 ± 0.02, and that of the normal and field cluster galaxies is $\sim 0.06 \pm 0.02$.

The red excess population is therefore characterized by high values of dust attenuation and SFR, suggesting the presence of dust-obscured star formation.
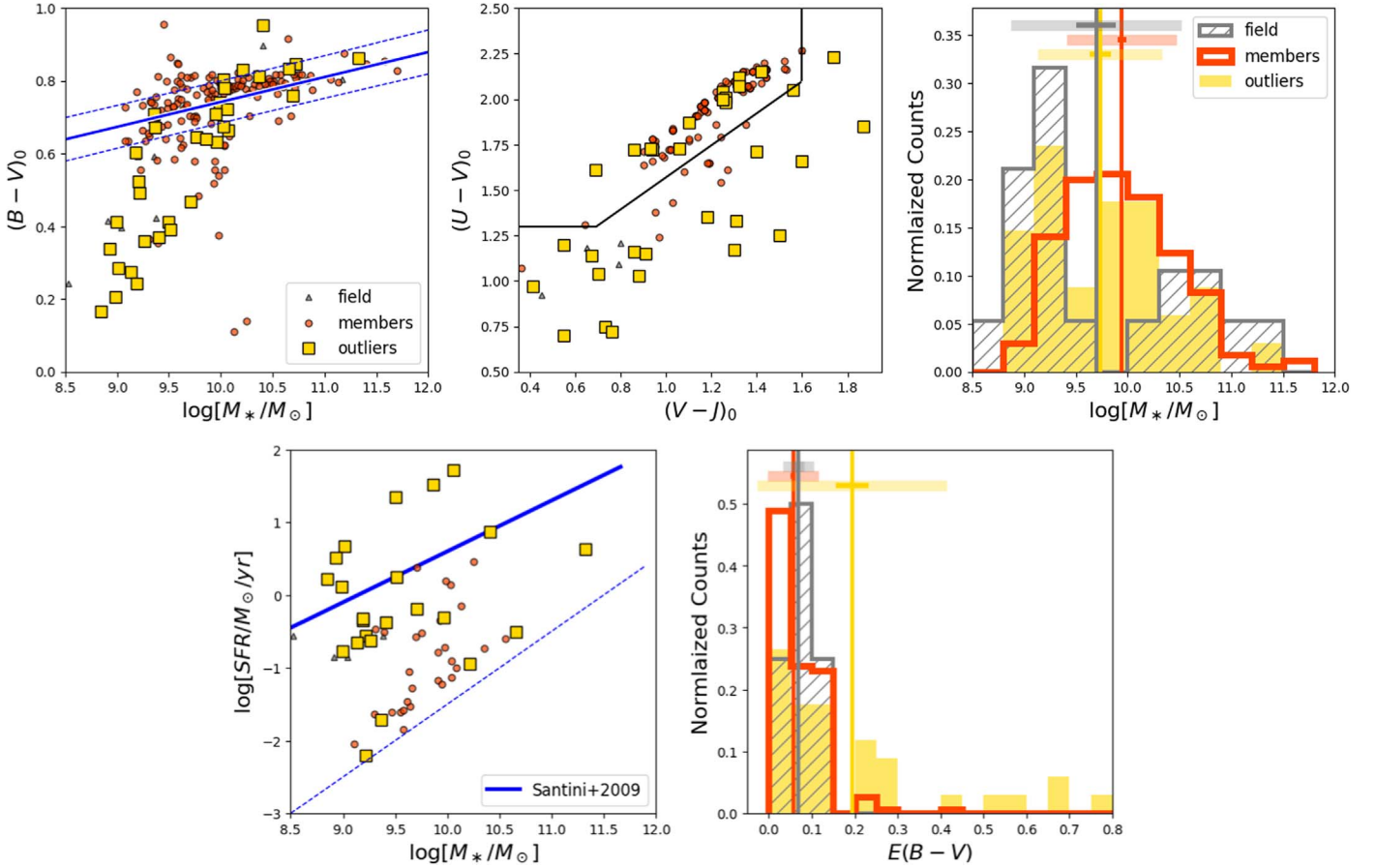
Figure 12. Top left: rest-frame $B - V$ vs. stellar mass for the normal cluster members (red circles), normal field galaxies (gray triangles), and red outliers (gold squares) identified in Section 5.1. The blue line represents the best fit of the red sequence, along with the 3σ scatter. Top middle: rest-frame $U - V$ vs. $V - J$ diagrams of the outliers, compared to normal field and cluster galaxies. Top right: stellar mass distribution for the different samples. Vertical lines show mean values; thick horizontal lines show the standard error of the distribution (lighter lines) and the error on the mean. Bottom left: SFR−mass relation for star-forming galaxies. The limit in sSFR (sSFR $> 10^{-11.5}$ yr^{-1}) is shown by the dashed blue line. The SFR−mass relation from Santini et al. (2009) in the redshift range $0.3 < z < 0.6$ is also plotted. Bottom right: $E(B - V)$ distribution for the different samples. Vertical lines show mean values; thick horizontal lines show the standard error of the distribution (lighter lines) and the error on the mean.
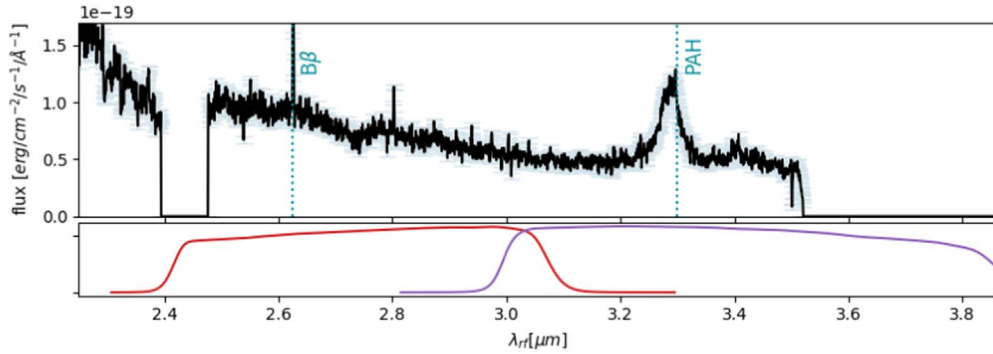
Figure 13. JWST/NIRSpec rest-frame spectrum for 41908, one of the galaxies in our sample characterized by extremely red colors. The position of the Brβ and of the PAH 3.3 μm is shown. There is no 3.05 μm water absorption, though, which is seen in spectra of some of the most dust-obscured galaxies. In the bottom panel, the corresponding bandpasses of the broadband F356W and F444W imaging filters are shown.

6.4. What Is the Origin of the Red Excess?

As part of the GLASS-JWST survey (ERS-1324, PI Treu; Treu et al. 2022b), we observed one red excess galaxy (41908) with JWST/NIRSpec in multiobject spectroscopy (MOS). We refer to Morishita et al. (2022) for details of the NIRSpec observations and data reduction. Figure 13 shows this spectrum shifted to the rest frame. Two lines are clearly visible: the most

prominent feature is the 3.3 μm polycyclic aromatic hydrocarbon (PAH) line, which has a rest-frame equivalent width (EW) of 590 ± 30 Å; in addition, the Brβ line is observed, with an emission EW of 30 ± 1 Å. The prominence of these lines can be responsible for the elevated fluxes measured in F356W and especially in F444W. The 3.3 μm PAH emission can place constraints on the contribution of dust-obscured star formation and active galactic nuclei (AGNs) to the cosmic IR background
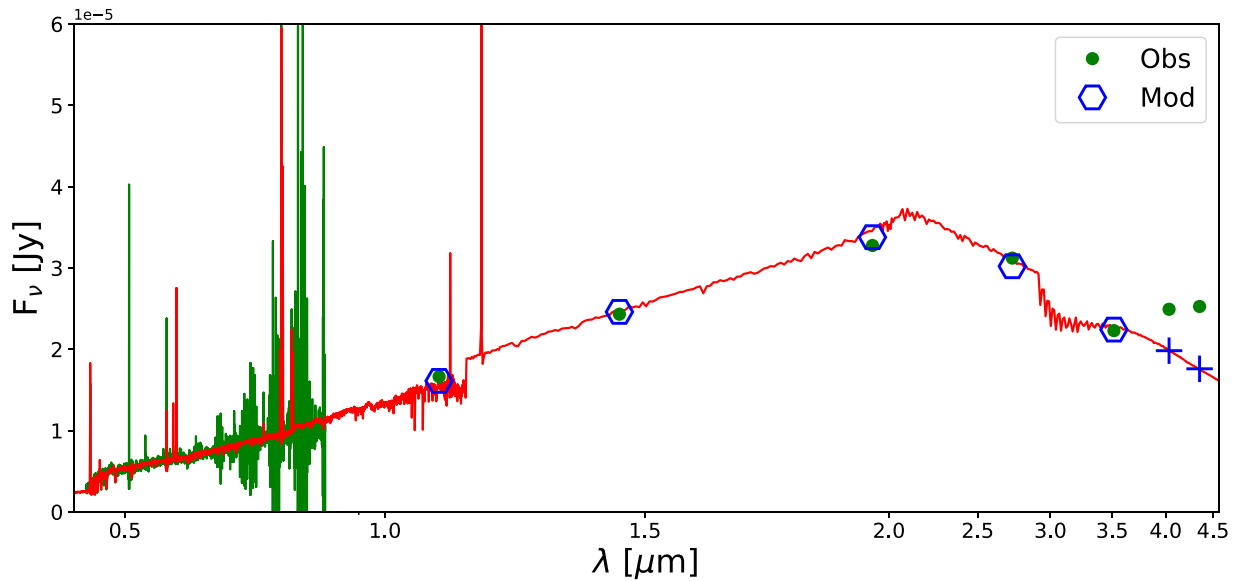
Figure 14. Example of the fitting obtained with the spectrophotometric modeling. The green line shows the observed MUSE spectrum, and the green points show the observed JWST/NIRCam photometry. Blue symbols show the values of the flux estimated by the model. Hexagons refer to the bands used in the modeling, and crosses refer to the bands excluded from the modeling. The red line shows the best fit.

(Schweitzer et al. 2006; Spoon et al. 2007; Teplitz et al. 2007; Valiante et al. 2007; Yan et al. 2007). The rest-frame EW of its 3.3 μm PAH line puts 41908 exactly at the boundary between "starburst-dominated" and "AGN-dominated" galaxy spectra (Inami et al. 2018). In general, PAH emission features are proposed to be an excellent indicator of star formation activity (e.g., Peeters et al. 2004; Brandl et al. 2006). PAHs are illuminated by UV photons, mostly from hot stars in star-forming regions (Boselli et al. 2004; Spoon et al. 2004; Calzetti 2011), while they are destroyed by hard radiation from an AGN central engine (Voit 1992).

In our sample, only two of the outliers have broad lines indicative of AGNs (70003981 and 70005765) in the MUSE spectra, while none of the other galaxies lie in the region occupied by AGNs in the BPT (Baldwin et al. 1981) diagram. Furthermore, another argument against an AGN origin is the fact that we found spatially extended F444W excesses, whereas the hot dust continuum in an AGN would only be present in the central unresolved nucleus. Thus, we hypothesize that the PAH observed in 41908 is due to heavily obscured star formation, as also suggested by the analysis of the SFR−mass relation and $E(B - V)$ distribution. A larger sample of NIR spectra will be needed to study in detail the origin of the red excess.

To quantify the amount of the red excess and test whether indeed the emission from stellar population is not enough to explain the observed flux, we combine the MUSE spectra with the JWST/NIRCam photometry, both extracted over the same aperture of $2\rlap{.}{''}24$, and fit the full SED with a set of templates that include the emission only from the stellar populations and not from the PAH.

We exploit the spectral synthesis code SImulatiNg OPtical Spectra wIth Stellar populations models (SINOPSIS; Fritz et al. 2007, 2011, 2017). SINOPSIS performs a nonparametric decomposition of galaxy spectra into a combination of single stellar population (SSP) models. The fit is performed by minimizing the difference between the model spectrum and the observed spectroscopic data, which include fluxes in selected continuum bands, and the EWs of both absorption and
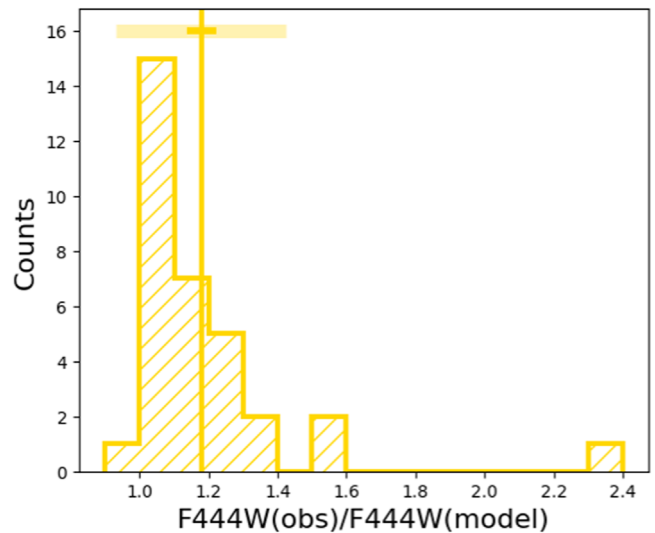

Figure 15. Ratio between the observed flux in F444W and the value obtained by the model for the red outliers. The vertical line shows the mean value, along with the standard deviation and the error on the mean.

emission lines (the latter consisting of Balmer lines and the [O II] λ3727 forbidden line, which are included in the SSP models; see Fritz et al. 2017, for a more detailed description). We also include JWST photometry as a constraint, and the model values are calculated by convolving the spectral model with the appropriate filter response curves. As we are interested in estimating the expected flux at F444W, under the assumption that all the observed emission comes from the pure stellar emission, we exclude this and (when available) the F410M band from the fitting. SINOPSIS combines SSPs of 11 different ages, with the oldest SSP age chosen to be consistent with a galaxy formation redshift of 20. We assume a constant value of the metallicity as a function of the stellar age, and seven different values were explored, from $Z = 0.001$ to 0.04. Figure 14 shows one example of the observed data and the best fit obtained by SINOPSIS.

From the best-fit model, we measure the expected F444W flux and compare it to the observed flux. The distribution of the observed to expected (model) ratios is reported in Figure 15. In all but one case the observed flux is indeed larger than what is predicted by the model. Typically, the observed value is 20% larger than the expected one, with one case where it is more than twice the expected value.

This analysis supports our working hypothesis based on only one NIRSpec spectrum that the observed excess is produced by warm/hot dust associated with intense star formation, and there is evidence for that in local starbursts (Calzetti et al. 2000). The presence of the 3.3 μm PAH, typically observed in actively star-forming galaxies, may play a significant role, even though its EW might not be high enough to lift up the entire broadband F444W filter flux of the observed values ($\sim$20%). The typical rest-frame EW of the 3.3 μm emission in star-forming galaxies is 0.1 μm. Thus, at a redshift of $z = 0.3$ it should only brighten the F444W filter by about 0.13 mag (and only by 0.20 mag for the most extreme PAH emitters in the GOALS sample; Inami et al. 2018). In addition, the PAH cannot be responsible for the observed boost in F356W and F410W, as it is outside the wavelength coverage of those filters. Larger spectroscopic samples targeting the PAH wavelength range are needed to better understand its role.

Alternatively, the excess could also be due to the presence of a deeply obscured AGN, whose presence is not unequivocally revealed by BPT line ratio diagrams. The hot dust emission rising from the dusty torus can contribute to an observed SED approximately at these wavelengths, producing an excess with respect to the pure stellar emission (see, e.g., Fritz et al. 2006). This scenario would explain particularly well those objects for which the excess is observed not only in the F444W band but also in the F410M one, as there are no known features to be held responsible for the simultaneous excess in the two bands. This hypothesis is, however, disfavored by the extent of the red emission, which in the case of AGNs should be point-like. Observations at longer wavelengths (rest frame 5–30 μm) would be critical to distinguish between these two scenarios.

In principle, none of the proposed scenarios, though, can fully explain the population of quiescent red outliers, unless they are also extremely obscured star-forming galaxies. Only spectra in the wavelength range of the F444W band could explain the origin of such red colors.

7. Summary and Conclusions

We combined JWST/NIRCam imaging and VLT/MUSE data to characterize the properties of galaxies in different environmental conditions in the cluster A2744 and in its immediate surroundings. We parameterized the environment in many different ways, to be sensitive to a wide range of mechanisms taking place in the cluster. Thanks to the red wavelength range covered by NIRCam data, we focused on the NIR properties of the galaxies, a so far poorly studied regime. The main results can be summarized as follows:

1. In the combined cluster and field sample, structural parameters have little dependence on wavelength: above $\lambda_{rf} > 0.9$ μm, the median difference between the Gini, M_{20}, concentration, clumpiness, and shape asymmetry parameters measured in the F444W band in any other band is consistent with zero. Consistent with previous results, morphologies in the NIR bands are rather constants (e.g., Elmegreen & Elmegreen 1981).

2. Galaxies in A2744 are characterized by a varieties of morphologies. Overall, E/S0/Sa galaxies dominate at all local densities, distances, surface mass densities, and the regions of past mergers. Our sample is too small to determine which of these parameterizations is the main driver.

3. A nonnegligible fraction ($\sim$17%) of galaxies with "red excess" F200W−F444W colors (up to 0.8 mag redder than red sequence galaxies) has been found to populate both the cluster regions and the field. Most of these galaxies are rather red also in the F200W−F356W color, even though the deviation is less pronounced. In contrast, they have typical F115W−F150W colors and rather blue rest-frame $B - V$ colors. Galaxies with the largest color deviations are found in the field and in the cluster outskirts, suggesting that mechanisms taking place in these regions might be more effective in producing these colors. These galaxies represent 50% of the total star-forming population, indicating that not all star-forming galaxies have such red colors. Many of them occupy the upper envelope of the SFR−mass relation and have high values of $E(B - V)$. Looking at their morphologies, many cluster galaxies have signatures typical of ram-pressure-stripped galaxies, while field galaxies have features resembling interaction and mergers.

This population of galaxies with the "red excess" resembles various populations of galaxies revealed by the Spitzer Space Telescope with significant excesses in their NIR emission, compared to what is expected from an old stellar population, at various redshifts (e.g., Papovich et al. 2007; Brand et al. 2009; Siana et al. 2009; Takagi et al. 2010). At $z \sim 0.3$, though, the PAH at 3.3 μm was outside the Spitzer window, so previous studies focused mainly on longer wavelengths. Brand et al. (2009) revealed a population of red sequence galaxies with a significant excess in their 24 μm emission and explained this excess in terms of the presence of strong 6.2 μm and 7.7 μm PAH emission features in their infrared spectra. They suggested that in a large fraction of the sources the infrared emission is dominated by star formation processes. Obscured star formation activity may be triggered by minor mergers of red galaxies or, in some cases, may be the residual activity as blue galaxies are quenched to form red sequence galaxies. However, no studies looked for an environmental dependency of this population.

The 3.3 μm PAH feature instead enters the [5.8] IRAC channel at $z > 0.6$, and Magnelli et al. (2008) have identified an IRAC excess in the SED of five galaxies, due to the predominance of this feature (see also Mentuch et al. 2009; Lange et al. 2016).

The red excess population also resembles the $z \sim 2$ submillimeter-selected galaxies discussed in Hainline et al. (2011). Fitting the observed-frame optical through mid-IR SEDs, they separated the stellar emission from nonstellar NIR continuum, finding that $\sim$10% of their galaxies have significant nonstellar contributions. Since the nonstellar continuum emission is correlated with hard X-ray luminosity, Hainline et al. (2011) concluded that AGNs are at the origin of the emission.

In line with the interpretation of the IRAC excesses, our hypothesis is that the galaxies discovered here are also

characterized by dust-enshrouded star formation (see also Smail et al. 1999; Duc et al. 2002): we analyzed a NIRSpec spectrum for one of the galaxies and found a strong PAH at 3.3 μm. This feature has often been used to trace dust-obscured star formation (e.g., Magnelli et al. 2008; Kim et al. 2012). Spectrophotometric modeling also supports this interpretation. On the other hand, this interpretation cannot fully explain the passive red excess galaxies, and no scenarios can currently explain them. Larger spectroscopic samples and spatially resolved spectra are, however, needed to understand whether the color excess is due exclusively to dust-obscured star formation, where in the galaxies the emission comes from, why not all star-forming galaxies are red outliers and why not all red outliers are star-forming, and the role of environment in triggering the color excess.

Facilities: JWST, MUSE/VLT

Software: astropy (Collaboration et al. 2018; Greenfield et al. 2013), grizli (Brammer & Matharu 2021)

ORCID iDs

Benedetta Vulcani ⓘ https://orcid.org/0000-0003-0980-1499
Tommaso Treu ⓘ https://orcid.org/0000-0002-8460-0390
Antonello Calabrò ⓘ https://orcid.org/0000-0003-2536-1614
Jacopo Fritz ⓘ https://orcid.org/0000-0002-7042-1965
Bianca M. Poggianti ⓘ https://orcid.org/0000-0001-8751-8360
Pietro Bergamini ⓘ https://orcid.org/0000-0003-1383-9414
Kristan Boyett ⓘ https://orcid.org/0000-0003-4109-304X
Gabriel B. Caminha ⓘ https://orcid.org/0000-0001-6052-3274
Marco Castellano ⓘ https://orcid.org/0000-0001-9875-8263
Alan Dressler ⓘ https://orcid.org/0000-0002-6317-0037
Adriano Fontana ⓘ https://orcid.org/0000-0003-3820-2823
Karl Glazebrook ⓘ https://orcid.org/0000-0002-3254-9044
Claudio Grillo ⓘ https://orcid.org/0000-0002-5926-7143
Matthew A. Malkan ⓘ https://orcid.org/0000-0001-6919-1237
Sara Mascia ⓘ https://orcid.org/0000-0002-9572-7813
Amata Mercurio ⓘ https://orcid.org/0000-0001-9261-7849
Emiliano Merlin ⓘ https://orcid.org/0000-0001-6870-8900
Benjamin Metha ⓘ https://orcid.org/0000-0002-8632-6049
Takahiro Morishita ⓘ https://orcid.org/0000-0002-8512-1404
Themiya Nanayakkara ⓘ https://orcid.org/0000-0003-2804-0648
Diego Paris ⓘ https://orcid.org/0000-0002-7409-8114
Guido Roberts-Borsani ⓘ https://orcid.org/0000-0002-4140-1367
Piero Rosati ⓘ https://orcid.org/0000-0002-6813-0632
Namrata Roy ⓘ https://orcid.org/0000-0002-4430-8846
Paola Santini ⓘ https://orcid.org/0000-0002-9334-8705
Michele Trenti ⓘ https://orcid.org/0000-0001-9391-305X
Eros Vanzella ⓘ https://orcid.org/0000-0002-5057-135X
Xin Wang ⓘ https://orcid.org/0000-0002-9373-3865

References

Abraham, R. G., van den Bergh, S., & Nair, P. 2003, ApJ, 588, 218
Andreon, S. 2013, A&A, 554, A79
Bacon, R., Conseil, S., Mary, D., et al. 2017, A&A, 608, A1
Baldwin, J. A., Phillips, M. M., & Terlevich, R. 1981, PASP, 93, 5
Balogh, M., Eke, V., Miller, C., et al. 2004, MNRAS, 348, 1355
Bellhouse, C., McGee, S. L., Smith, R., et al. 2021, MNRAS, 500, 1285
Bellhouse, C., Poggianti, B., Moretti, A., et al. 2022, ApJ, 937, 18
Bergamini, P., Acebron, A., Grillo, C., et al. 2023a, A&A, 670, A60
Bergamini, P., Acebron, A., Grillo, C., et al. 2023b, arXiv:2303.10210
Bezanson, R., Labbe, I., Labbe, K. E., et al. 2022, arXiv:2212.04026
Bohlin, R. C., Cornett, R. H., Hill, J. K., et al. 1991, ApJ, 368, 12
Boschin, W., Girardi, M., Spolaor, M., & Barrena, R. 2006, A&A, 449, 461
Boselli, A., & Gavazzi, G. 2006, PASP, 118, 517
Boselli, A., Lequeux, J., & Gavazzi, G. 2004, A&A, 428, 409
Brammer, G., & Matharu, J. 2021, gbrammer/grizli: Release 2021, v1.3.2, Zenodo, doi:10.5281/zenodo.5012699
Brand, K., Moustakas, J., Armus, L., et al. 2009, ApJ, 693, 340
Brandl, B. R., Bernard-Salas, J., Spoon, H. W. W., et al. 2006, ApJ, 653, 1129
Bruzual, G., & Charlot, S. 2003, MNRAS, 344, 1000
Butcher, H., & Oemler, A., Jr+ 1984, ApJ, 285, 426
Calabrò, A., Daddi, E., Fensch, J., et al. 2019, A&A, 632, A98
Calvi, R., Poggianti, B. M., Fasano, G., & Vulcani, B. 2012, MNRAS, 419, L14
Calzetti, D. 2011, EAS Publ., 46, 133
Calzetti, D., Armus, L., Bohlin, R. C., et al. 2000, ApJ, 533, 682
Caminha, G. B., Grillo, C., Rosati, P., et al. 2017, A&A, 600, A90
Caminha, G. B., Rosati, P., Grillo, C., et al. 2019, A&A, 632, A36
Castellano, M., Sommariva, V., Fontana, A., et al. 2014, A&A, 566, A19
Chabrier, G. 2003, PASP, 115, 763
Collaboration, A., Price-Whelan, A. M., Sipőcz, B. M., et al. 2018, AJ, 156, 123
Conselice, C. J. 2003, ApJS, 147, 1
Conselice, C. J. 2014, ARA&A, 52, 291
Couch, W. J., Newell, E. B., Couch, W. J., & Newell, E. B. 1984, ApJS, 56, 143
Couch, W. J., & Sharples, R. M. 1987, MNRAS, 229, 423
De Lucia, G., Poggianti, B. M., Aragón-Salamanca, A., et al. 2004, ApJL, 610, L77
Dressler, A. 1980, ApJ, 236, 351
Dressler, A., Oemler, A., Jr., Couch, W. J., et al. 1997, ApJ, 490, 577
Duc, P. A., Poggianti, B., Elbaz, D. F. D., et al. 2002, A&A, 382, 60
Elmegreen, D. M., & Elmegreen, B. 1981, ApJS, 47, 229
Fasano, G., Poggianti, B. M., Bettoni, D., et al. 2015, MNRAS, 449, 3927
Fontana, A., D'Odorico, S., Poli, F., et al. 2000, AJ, 120, 2206
Fritz, J., Franceschini, A., & Hatziminaoglou, E. 2006, MNRAS, 366, 767
Fritz, J., Moretti, A., Gullieuszik, M., et al. 2017, ApJ, 848, 132
Fritz, J., Poggianti, B. M., Bettoni, D., et al. 2007, A&A, 470, 137
Fritz, J., Poggianti, B. M., Cava, A., et al. 2011, A&A, 526, A45
Gao, L., Springel, V., & White, S. D. M. 2005, MNRAS, 363, L66
Girardi, M., & Mezzetti, M. 2000, ApJ, 548, 79

Greenfield, P., Robitaille, T., Tollerud, E., et al. 2013, Astrophysics Source Code Library, record ascl:1304.002
Gullieuszik, M., Poggianti, B. M., McGee, S. L., et al. 2020, ApJ, 889, 13
Hainline, L. J., Blain, A. W., Smail, I., et al. 2011, ApJ, 740, 96
Hashimoto, Y., Oemler, A., Jr., Lin, H., & Tucker, D. L. 1998, ApJ, 499, 589
Ilbert, O., McCracken, H. J., Le Fevre, O., et al. 2013, A&A, 556, A55
Inami, H., Armus, L., Matsuhara, H., et al. 2018, A&A, 617, 130
Jaffé, Y., Poggianti, B., Moretti, A., et al. 2018, MNRAS, 476, 4753
Jauzac, M., Eckert, D., Schwinn, J., et al. 2016, MNRAS, 463, 3876
Kelkar, K., Gray, M. E., Aragón-Salamanca, A., et al. 2019, MNRAS, 486, 868
Kempner, J. C., & David, L. P. 2003, MNRAS, 349, 385
Kim, J. H., Im, M., Lee, H. M., et al. 2012, ApJ, 760, 120
Kron, R. G. 1980, ApJS, 43, 305
Kuchinski, L. E., Freedman, W. L., Madore, B. F., et al. 2000, ApJS, 131, 441
Labbé, I., Huang, J., Franx, M., et al. 2005, ApJL, 624, L81
Lange, J. U., van Dokkum, P. G., Momcheva, I. G., et al. 2016, ApJ, 819, L4
Lewis, I., Balogh, M., De Propris, R., et al. 2002, MNRAS, 334, 673
Lotz, J. M., Davis, M., Faber, S. M., et al. 2008, ApJ, 672, 177
Lotz, J. M., Primack, J., & Madau, P. 2004, AJ, 128, 163
Magnelli, B., Chary, R. R., Pope, A., et al. 2008, ApJ, 681, 258
Markevitch, M., Forman, W. R., Sarazin, C. L., & Vikhlinin, A. 1998, ApJ, 503, 77
Mastropietro, C., Moore, B., Mayer, L., et al. 2005, MNRAS, 364, 607
Maulbetsch, C., Avila-Reese, V., Colin, P., et al. 2007, ApJ, 654, 53
Mentuch, E., Abraham, R. G., Glazebrook, K., et al. 2009, ApJ, 706, 1020
Merlin, E., Bonchi, A., Paris, D., et al. 2022, ApJL, 938, L14
Merlin, E., Castellano, M., Santini, P., et al. 2021, A&A, 649, A22
Mihos, J. C., & Hernquist, L. 1996, ApJ, 464, 641
Moretti, A., Radovich, M., Poggianti, B. M., et al. 2022, ApJ, 925, 4
Morishita, T., Abramson, L. L. E., Treu, T., et al. 2016, ApJ, 835, 254
Morishita, T., Roberts-Borsani, G., Treu, T., et al. 2022, arXiv:2211.09097
Muzzin, A., Marchesini, D., Stefanon, M., et al. 2013, ApJ, 777, 18
Newman, A. B., Ellis, R. S., Andreon, S., et al. 2014, ApJ, 788, 51
Owers, M. S., Couch, W. J., Nulsen, P. E. J., & Randall, S. W. 2012, ApJL, 750, L23
Owers, M. S., Randall, S. W., Nulsen, P. E., et al. 2011, ApJ, 728, 27
Paccagnella, A., Vulcani, B., Poggianti, B. M., et al. 2016, ApJL, 816, L25
Papovich, C., Bassett, R., Lotz, J. M., et al. 2012, ApJ, 750, 93
Papovich, C., Rudnick, G., Le Floc'h, E., et al. 2007, ApJ, 668, 45
Paris, D., Merlin, E., Fontana, A., et al. 2023, arXiv:2301.02179
Pasquali, A., Smith, R., Gallazzi, A., et al. 2019, MNRAS, 484, 1702
Pawlik, M. M., Wild, V., Walcher, C. J., et al. 2016, MNRAS, 456, 3
Peeters, E., Spoon, H. W. W., & Tielens, A. G. G. M. 2004, ApJ, 613, 986
Peng, Y.-j., Lilly, S. J., Kovač, K., et al. 2010, ApJ, 721, 193
Poggianti, B. M., von der Linden, A., De Lucia, G., et al. 2006, ApJ, 642, 188
Postman, M., Franx, M., Cross, N. J. G., et al. 2005, ApJ, 623, 721

Postman, M., & Geller, M. J. 1984, ApJ, 281, 95
Prieto-Lyon, G., Strait, V., Mason, C. A., et al. 2022, arXiv:2211.12548
Rawle, T. D., Altieri, B., Egami, E., et al. 2014, MNRAS, 442, 196
Rhee, J., Smith, R., Choi, H., et al. 2017, ApJ, 843, 128
Richard, J., Claeyssens, A., Lagattuta, D., et al. 2021, A&A, 646, A83
Rudnick, G. H., Tran, K. V., Papovich, C., Momcheva, I., & Willmer, C. 2012, ApJ, 755, 14
Santini, P., Fontana, A., Castellano, M., et al. 2023, ApJL, 942, L27
Santini, P., Fontana, A., Grazian, A., et al. 2009, A&A, 504, 751
Schaerer, D., & De Barros, S. 2009, A&A, 502, 423
Schweitzer, M., Lutz, D., Sturm, E., et al. 2006, ApJ, 649, 79
Shankar, F., Marulli, F., Bernardi, M., et al. 2013, MNRAS, 428, 109
Sheen, Y.-K., Smith, R., Jaffé, Y., et al. 2017, ApJL, 840, L7
Siana, B., Smail, I., Swinbank, A. M., et al. 2009, ApJ, 698, 1273
Smail, I., Morrison, G. E., Gray, M. E., et al. 1999, ApJ, 525, 609
Smith, R., Sánchez-Janssen, R., Beasley, M. A., et al. 2015, MNRAS, 454, 2502
Song, H., Hwang, H. S., Park, C., & Tamura, T. 2017, ApJ, 842, 88
Spoon, H. W., Moorwood, A. F., Lutz, D., et al. 2004, A&A, 414, 873
Spoon, H. W. W., Marshall, J. A., Houck, J. R., et al. 2007, ApJL, 654, L49
Straatman, C. M., Labbé, I., Spitler, L. R., et al. 2014, ApJL, 783, L14
Straatman, C. M. S., Spitler, L. R., Quadri, R. F., et al. 2016, ApJ, 830, 51
Takagi, T., Ohyama, Y., Goto, T., et al. 2010, A&A, 514, 13
Teplitz, H. I., Desai, V., Armus, L., et al. 2007, ApJ, 659, 941
Treu, T., Calabro, A., Castellano, M., et al. 2023, ApJL, 942, L28
Treu, T., Roberts-Borsani, G., Bradac, M., et al. 2022, ApJ, 935, 110
Valentinuzzi, T., Poggianti, B. M., Fasano, G., et al. 2011, A&A, 536, A34
Valiante, E., Lutz, D., Sturm, E., et al. 2007, ApJ, 660, 1060
Voit, G. M. 1992, MNRAS, 258, 841
von der Linden, A., Wild, V., Kauffmann, G., White, S. D. M., & Weinmann, S. 2010, MNRAS, 404, 1231
Vulcani, B., Poggianti, B. M., Aragón-Salamanca, A., et al. 2011, MNRAS, 412, 246
Vulcani, B., Poggianti, B. M., Finn, R. A., et al. 2010, ApJL, 710, L1
Vulcani, B., Poggianti, B. M., Gullieuszik, M., et al. 2018, ApJL, 866, L25
Vulcani, B., Poggianti, B. M., Gullieuszik, M., et al. 2023, arXiv:2302.02376
Vulcani, B., Poggianti, B. M., Smith, R., et al. 2022, ApJ, 927, 91
Vulcani, B., Treu, T., Nipoti, C., et al. 2017, ApJ, 837, 126
Weaver, J. R., Cutler, S. E., Pan, R., et al. 2023, arXiv:2301.02671
Webb, K., Balogh, M. L., Leja, J., et al. 2020, MNRAS, 498, 5317
Werle, A., Poggianti, B., Moretti, A., et al. 2022, ApJ, 930, 43
Whitaker, K. E., Labbé, I., van Dokkum, P. G., et al. 2011, ApJ, 735, 86
Williams, R. J., Quadri, R. F., Franx, M., van Dokkum, P., & Labbé, I. 2009, ApJ, 691, 1879
Windhorst, R. A., Taylor, V. A., Jansen, R. A., et al. 2002, ApJS, 143, 113
Yan, L., Sajina, A., Fadda, D., et al. 2007, ApJ, 658, 778